A&A 519, A17 (2010)
DOI: 10.1051/0004-6361/201014320

Astronomy & Astrophysics

Variability and the X-ray/UV ratio of active galactic nuclei⋆

F. Vagnetti[1], S. Turriziani[1,⋆⋆], D. Trevese[2], and M. Antonucci[1]

[1] Dipartimento di Fisica, Università di Roma "Tor Vergata", via della Ricerca Scientifica 1, 00133 Roma, Italy
e-mail: fausto.vagnetti@roma2.infn.it
[2] Dipartimento di Fisica, Università di Roma "La Sapienza", Piazzale Aldo Moro 2, 00185 Roma, Italy

Received 25 February 2010 / Accepted 27 April 2010

ABSTRACT

Context. The observed relation between the X-ray radiation from active galactic nuclei, originating in the corona, and the optical/UV radiation from the disk is usually described by the anticorrelation between the UV to X-ray slope α_{ox} and the UV luminosity. Many factors can affect this relation, including: i) enhanced X-ray emission associated with the jets of radio-loud AGNs, ii) X-ray absorption associated with the UV broad absorption line (BAL) outflows, iii) other X-ray absorption not associated with BALs, iv) intrinsic X-ray weakness, v) UV and X-ray variability, and non-simultaneity of UV and X-ray observations. The separation of these effects provides information about the intrinsic $\alpha_{ox} - L_{UV}$ relation and its dispersion, constraining models of disk-corona coupling.
Aims. We use simultaneous UV/X-ray observations to remove the influence of non-simultaneous measurements from the $\alpha_{ox} - L_{UV}$ relation.
Methods. We extract simultaneous data from the second *XMM-Newton* serendipitous source catalogue (XMMSSC) and the *XMM-Newton* Optical Monitor Serendipitous UV Source Survey catalogue (XMMOMSUSS), and derive the single-epoch α_{ox} indices. We use ensemble structure functions to analyse multi-epoch data.
Results. We confirm the anticorrelation of α_{ox} with L_{UV}, and do not find any evidence of a dependence of α_{ox} on z. The dispersion in our simultaneous data ($\sigma \sim 0.12$) is not significantly smaller than in previous non-simultaneous studies, suggesting that "artificial α_{ox} variability" introduced by non-simultaneity is not the main cause of dispersion. "Intrinsic α_{ox} variability", i.e., the true variability of the X-ray to optical ratio, is instead important, and accounts for ∼30% of the total variance, or more. "Inter-source dispersion", due to intrinsic differences in the average α_{ox} values from source to source, is also important. The dispersion introduced by variability is mostly caused by the long timescale variations, which are expected to be driven by the optical variations.

Key words. surveys – galaxies: active – quasars: general - X-rays: galaxies

1. Introduction

The relationship between the X-ray and optical/UV luminosity of active galactic nuclei (AGNs) is usually described in terms of the index $\alpha_{ox} = 0.3838 \log(L_X/L_{UV})$, i.e., the slope of a hypothetical power law between 2500 Å and 2 keV rest-frame frequencies. The X-ray and UV monochromatic luminosities are correlated over 5 decades as $L_X \propto L_{UV}^k$, with $k \sim 0.5$–0.7, and this provides an anticorrelation $\alpha_{ox} = a \log L_{UV} + \text{const}$, with $-0.2 \lesssim a \lesssim -0.1$ (e.g., Avni & Tananbaum 1986; Vignali et al. 2003; Strateva et al. 2005; Steffen et al. 2006; Just et al. 2007; Gibson et al. 2008). One of the main results of these analyses is that QSOs are universally X-ray luminous and that X-ray weak QSOs are very rare (e.g., Avni & Tananbaum 1986; Gibson et al. 2008), but it is not yet known if the same is true for moderate luminosity AGNs. UV photons are generally believed to be radiated from the QSO accretion disk, while X-rays are supposed to originate in a hot coronal gas of unknown geometry and disk-covering fraction. The X-ray/UV ratio provides information about the balance between the accretion disk and the corona, which is not yet understood in detail. The $\alpha_{ox} - L_{UV}$ anticorrelation implies that AGNs redistribute their energy in the UV and X-ray bands depending on the overall luminosity, with more luminous AGNs emitting fewer X-rays per unit UV luminosity than less luminous AGNs (Strateva et al. 2005). It has been proposed that the anticorrelation can be caused by the larger dispersion in the luminosities in the UV than the X-ray band for a population with intrinsically uniform α_{ox} (La Franca et al. 1995; Yuan et al. 1998); however, more recent analyses based on samples with wider luminosity ranges confirm the reality of the relationship (Strateva et al. 2005). Gibson et al. (2008) stressed the quite large scatter in the X-ray brightness of individual sources about the average relation and investigated the possible causes of the dispersion. Part of this scatter, usually removed (e.g., Strateva et al. 2005; Steffen et al. 2006; Just et al. 2007; Gibson et al. 2008) is caused by radio-loud quasars, which are relatively X-ray bright because of the enhanced X-ray emission associated with their jets (e.g., Worrall et al. 1987), and to broad absorption line (BAL) quasars, which are relatively X-ray faint (e.g., Brandt et al. 2000) due to X-ray absorption associated with the UV BAL outflows. Additional causes of deviations from the average $\alpha_{ox} - L_{UV}$ relation include: i) X-ray absorption not associated with BALs, ii) intrinsic X-ray weakness, and iii) UV and X-ray variability, possibly in association with non-simultaneous UV and X-ray observations. In particular, Gibson et al. (2008) estimate that variability may be responsible for 70%–100% of the α_{ox} dispersion, and that a few percent (<2%) of all quasars are intrinsically X-ray weak by a factor of 10, compared to the average value at the same UV luminosity. A large fraction of intrinsically X-ray weak sources would

⋆ Table 1 is only available in electronic form at http://www.aanda.org
⋆⋆ Visitor at ASI Science Data Center, via Galileo Galilei, 00044 Frascati, Italy.

suggest that coronae may frequently be absent or disrupted in QSOs. An extreme case is PHL 1811, which is X-ray weak by a factor ~70, studied in detail by Leighly et al. (2007), who propose various scenarios, including disk/corona coupling by means of magnetic reconnections, Compton cooling of the corona by unusually soft optical/UV spectrum, and the photon trapping of X-ray photons and their advection to the black hole. The influence of variability on the $\alpha_{ox} - L_{UV}$ relation can be divided into two different effects: i) non-simultaneity of X-ray and UV measurements, which we call "artificial α_{ox} variability", and ii) true variability in the X-ray/UV ratio, which we refer to as "intrinsic α_{ox} variability". It is beneficial to analyse simultaneously acquired X-ray and UV data to eliminate the effect of the artificial variability and search for the intrinsic X-ray/UV ratio and/or its variability. On a rest-frame timescale of a few years, the optical/UV variability of QSOs has been estimated to be ~30% (e.g., Giallongo et al. 1991; Vanden Berk et al. 2004), while X-ray variability has been estimated to be ~40% for Seyfert 1 AGNs (Markowitz et al. 2003). On intermediate timescales, the relation between X-ray and optical/UV variability may be due to either: i) the reprocessing of X-rays into thermal optical emission, by means of irradiation and heating of the accretion disk, or ii) Compton up-scattering, in the hot corona, of optical photons emitted by the disk. In the former case, variations in the X-ray flux would lead optical/UV ones, and vice versa in the latter case. Cross-correlation analyses of X-ray and optical/UV light curves allow us to constrain models for the origin of variability. The main results obtained so far, on the basis of simultaneous X-ray and optical observations, indicate a cross-correlation between X-ray and UV/optical variation on the timescale of days, and in some cases delays of the UV ranging from 0.5 to 2 days have been measured (Smith & Vaughan 2007). Simultaneous X-ray/UV data can be obtained by the *XMM-Newton* satellite, which carries the co-aligned Optical Monitor (OM). The second *XMM-Newton* serendipitous source catalogue (XMMSSC) (Watson et al. 2009) is available online in the updated incremental version 2XMMi[1]. The *XMM-Newton* Optical Monitor Serendipitous UV Source Survey catalogue (XMMOMSUSS) is also available online[2]. We look for simultaneous measurements of the α_{ox} index from XMM/OM catalogues, to provide at least partial answers to the following questions: how large is the effect of non-simultaneous X-ray/UV observations on the dispersion about the average $\alpha_{ox} - L_{UV}$ relationship? Is there any spectral X-UV variability for individual objects? Do their α_{ox} harden in the bright phases or vice versa? Which constraints do these measurements place on the relationship between the accretion disk and the corona?

The paper is organised as follows. Section 2 describes the data extracted from the archival catalogues. Section 3 describes the SEDs of the sources and the evaluation of the specific UV and X-ray luminosities. Section 4 discusses the $\alpha_{ox} - L_{UV}$ anticorrelation and its dispersion. In Sect. 5, we present the multi-epoch data and discuss the intrinsic X/UV variability of individual sources. Section 6 provides notes about individual peculiar sources. Section 7 discusses and summarises the results.

Throughout the paper, we adopt the cosmology $H_0 = 70\ \mathrm{km\,s^{-1}\,Mpc^{-1}}$, $\Omega_m = 0.3$, and $\Omega_\Lambda = 0.7$.

[1] http://heasarc.gsfc.nasa.gov/W3Browse/xmm-newton/xmmssc.html

[2] http://heasarc.gsfc.nasa.gov/W3Browse/xmm-newton/xmmomsuss.html

2. The data

The updated incremental version 2XMMi of the second *XMM-Newton* serendipitous source catalogue (XMMSSC) (Watson et al. 2009) is available online and contains 289 083 detections between 2000 February 3 and 2008 March 28[3]. The net sky area covered by the catalogue fields is ~360 deg^2.

XMMOMSUSS is a catalogue of UV sources detected serendipitously by the Optical Monitor (OM) onboard the *XMM-Newton* observatory and is a partner resource to the 2XMM serendipitous X-ray source catalogue. The catalogue contains source detections drawn from 2417 XMM-OM observations in up to three broad-band UV filters, performed between 2000 February 24 and 2007 March 29. The net sky area covered is between 29 and 54 square degrees, depending on UV filter. The XMMOMSUSS catalogue contains 753 578 UV source detections above a signal-to-noise ratio threshold limit of 3-σ, which relate to 624049 unique objects.

We first correlated the XMMSSC with the XMMOMSUSS catalogue to search for X-ray and UV sources with a maximum separation of 1.5 arcsec, corresponding to ~1σ uncertainty in the X-ray position. This yields 22061 matches. To obtain simultaneous X-ray and UV data, we searched for data from the same *XMM-Newton* observations, comparing the parameters OBS_ID and OBSID of the XMMSSC and XMMOMSUSS catalogue, respectively, that identify uniquely the *XMM-Newton* pointings. This reduces the set to 8082 simultaneous observations. For the correlations, we used the Virtual Observatory application TOPCAT[4].

We then correlated this table with the Sloan Digital Sky Survey (SDSS) Quasar Catalogue, Data Release 5, to provide optical classifications and redshifts for the matched objects (Schneider et al. 2007). Using again a maximum distance of 1.5 arcsec (uncertainty in the X-ray position), we found 310 matches. Increasing the maximum distance up to 5 arcsec, we add only 5 matches, none of which has a separation >2 arcsec. This indicates that, in spite of the relatively small (1.5 arcsec ~ 1σ) cross-correlation radius adopted to reduce the contamination, the resulting incompleteness (at the present flux limit) is negligible. The X-ray to optical ratios of the added 5 sources are not peculiar, therefore we used the entire sample of 315 matches. This also includes multi-epoch data for 46 sources (from 2 to 9 epochs each) and single-epoch observations for 195 more sources, for a total number of 241 sources.

To estimate the probability of false identifications, we applied an arbitrary shift of 1 arcmin in declination to the X-ray coordinates of the 8082 simultaneous observations, and we found 219 UV/X-ray spurious associations, i.e., 2.7%. This would correspond to ~ 8 spurious matches among the 315 observations of our final sample.

The relevant data of the sources are reported in Table 1, where: Col. 1 corresponds to the source serial number; Col. 2, the observation epoch serial number; Col. 3 source name; Col. 4 epoch (MJD); Col. 5 redshift; Col. 6 radio-loud flag (1=radio-loud, 0=radio-quiet, -1=unclassified); Col. 7 BAL flag (1=BAL, 0=non-BAL); Col. 8 log of the specific luminosity at 2500 Å

[3] After the submission of the article, a note has been distributed about "Incorrect EPIC band-4 fluxes in the 2XMM and 2XMMi catalogues" (*XMM-Newton* News #105, http://xmm.esac.esa.int/external/xmm_news/news_list/). This affects 83 observations among the 315 in Table 1, which is corrected in agreement with the new data released by the *XMM-Newton* Survey Science Centre. All our analysis is also corrected with the new data.

[4] http://www.star.bris.ac.uk/~mbt/topcat/

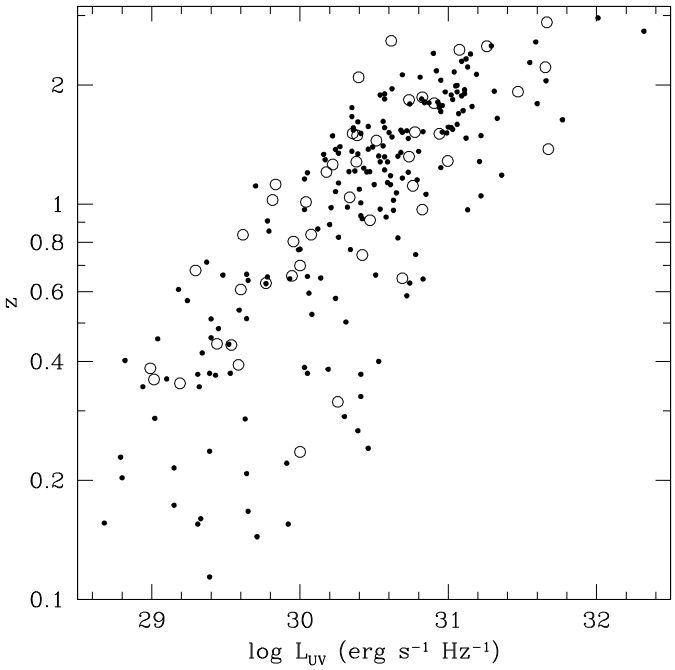

Fig. 1. The sources in the luminosity-redshift plane. All the sources in Table 1 are reported. Small dots correspond to single-epoch data, while open circles indicate average luminosity values of multi-epoch sources.

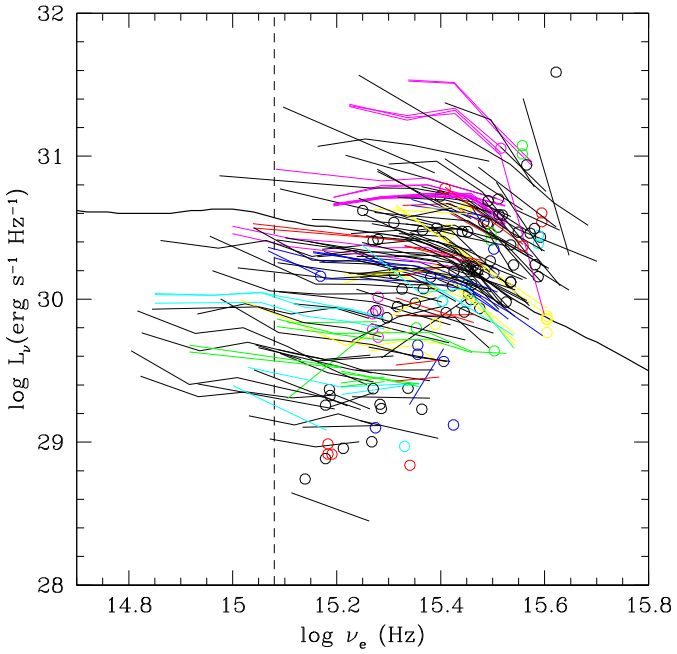

Fig. 2. Spectral energy distributions from the available OM data. Sources with 2 or more frequency points are shown as lines, while small circles represent sources with only 1 frequency point. Black lines and circles refer to sources with data at a single epoch, while coloured data refer to multi-epoch sources. Data from the same source are plotted with the same colour, but more sources are represented with the same colour. The continuous curve covering all the range of the plot is the average SED computed by Richards et al. (2006) for type 1 quasars from the SDSS.

in erg s^{-1} Hz^{-1}; Col. 9 log of the specific luminosity at 2 keV in erg s^{-1} Hz^{-1}; Col. 10 UV to X-ray power law index α_{ox}; Col. 11 residual of α_{ox} w.r.t. the adopted α_{ox}-L_{UV} correlation; and Col. 12 hardness ratio between the bands 1−2 keV and 2−4.5 keV.

The sources span a region in the luminosity-redshift plane with $0.1 \lesssim z \lesssim 3$ and 10^{29} erg s^{-1} Hz^{-1} $\lesssim L_{UV} \lesssim$ 10^{32} erg s^{-1} Hz^{-1}, as shown in Fig. 1.

3. Evaluation of the specific luminosities

3.1. UV

The Optical Monitor onboard *XMM-Newton* is described in detail in Mason et al. (2001). The set of filters included within the XMMOMSUSS catalogue is described in a dedicated page at MSSL[5]. The filters are called *UVW2*, *UVM2*, *UVW1*, *U*, *B*, and *V*, with central wavelengths 1894 Å, 2205 Å, 2675 Å, 3275 Å, 4050 Å, and 5235 Å, respectively. The last three filters are similar, but not identical, to the Johnson UBV set.

In the evaluation of the rest-frame luminosities, it is inadvisable to apply k-corrections using fixed power laws, because the local slope of the power law[6] at the emission frequency corresponding to the observed bandpasses changes as a function of the source redshift, between ∼−0.5 and ∼−2 (see, e.g., Richards et al. 2006). The effective slope to compute specific luminosity at 2500 Å is an appropriate average of the slopes between the emission frequency and the frequency corresponding to 2500 Å.

One or more specific fluxes, up to six, are reported in XMMOMSUSS for the filters effectively used for each source, depending on observational limitations at each pointing. We were therefore able to compute optical-UV spectral energy distributions (SEDs) for each source. We derived specific luminosities at the different emission frequencies of the SEDs according to the classical formula

$$L_\nu(\nu_e) = F_\nu(\nu_o)\frac{4\pi D_L^2}{1+z} \cdot \quad (1)$$

The result is plotted in Fig. 2, where SEDs with 2−6 frequency points are shown as lines, while small circles represent sources with only 1 frequency point. Black lines and circles refer to sources with data at a single epoch, while colours are used for multi-epoch sources. Data from the same source are plotted with the same colour, but more sources are represented with the same colour. The continuous curve covering the entire range of the plot is the average SED computed by Richards et al. (2006) for type 1 quasars from the SDSS.

The specific luminosity at 2500 Å, ($\log \nu_e = 15.08$), called L_{UV} for brevity, is evaluated as follows: i) if the SED of the source extends across a sufficiently wide range at low frequency, crossing the $\log \nu_e = 15.08$ line (see Fig. 2), L_{UV} is computed as an interpolation of the SED values in the 2 nearest frequency points; ii) in the other cases, i.e., if $\log \nu_e > 15.08$ for all the SED, we use a curvilinear extrapolation, adopting the shape of the average SED by Richards et al. (2006), shifting it vertically to match the specific luminosity of the source at the lowest frequency point available, say ν_1, and applying a correction factor between $\log \nu_1$ and 15.08. Another possibility would be to extrapolate the source's SED using a power law with the same slope as that between the two lowest frequency points, but this is not applicable when there is only 1 frequency point, and is inappropriate when $\log \nu_1 \gtrsim 15.3$, because it is then in a region where

[5] http://www.mssl.ucl.ac.uk/~mds/XMM-OM-SUSS/SourcePropertiesFilters.shtml.

[6] We adopt spectral indices following the implicit sign convention, $L_\nu \propto \nu^\alpha$.

the average SED by Richards et al. (2006) steepens. We therefore do not apply this power law extrapolation, and use instead the curvilinear extrapolation (ii) described above. However, we tested the use of this power law extrapolation for the subset of SEDs for which it can be applied, and computed the $\alpha_{ox} - L_{UV}$ relation as described in the following (Sect. 4). We found similar slopes (within 0.010) and dispersions (within 0.005), which does not influence our final conclusions.

3.2. X-ray

X-ray fluxes are provided by the XMMSSC catalogue integrated in 5 basic energy bands, 0.2–0.5 keV (band 1), 0.5–1 keV (band 2), 1–2 keV (band 3), 2–4.5 keV (band 4), and 4.5–12 keV (band 5) (Watson et al. 2009). Power law distributions with photon index[7] $\Gamma = 1.7$ and absorbing column density $N_H = 3 \times 10^{20}$ cm^{-2} are assumed in the computation of the fluxes.

To evaluate the specific luminosity at 2 keV (which we call L_X for brevity), we can use the flux in one of the two adjacent bands, 3 or 4. Since the fluxes are computed with negligible absorption, we prefer to use the band 4, which is less absorbed than the band 3 in type-2 obscured AGNs. It would also be possible to directly measure rest-frame 2 keV flux from observed low-energy bands 1 or 2, but – again – this would provide in some cases an absorbed flux. We therefore use the power law integral

$$F_X(2\text{–}4.5\,\mathrm{keV}) = \int_{2\,\mathrm{keV}}^{4.5\,\mathrm{keV}} F_\nu(2\,\mathrm{keV}) \left(\frac{\nu}{\nu_{2\,\mathrm{keV}}}\right)^{1-\Gamma} \mathrm{d}\nu \qquad (2)$$

and determine the specific flux at 2 keV (observed frame) to be:

$$F_\nu(2\,\mathrm{keV}) = \frac{F_X(2\text{–}4.5\,\mathrm{keV})}{\nu_{2\,\mathrm{keV}}} \frac{2-\Gamma}{2.25^{2-\Gamma}-1}\,. \qquad (3)$$

We then apply a standard power law k-correction

$$L_\nu(2\,\mathrm{keV}) = F_\nu(2\,\mathrm{keV}) \frac{4\pi D_L^2}{(1+z)^{2-\Gamma}}, \qquad (4)$$

adopting $\Gamma = 1.7$ as assumed in the catalogue.

4. The α_{ox}–L_{UV} anticorrelation

We define, as usual

$$\alpha_{ox} = \frac{\log(L_{2\,\mathrm{keV}}/L_{2500\,\text{Å}})}{\log(\nu_{2\,\mathrm{keV}}/\nu_{2500\,\text{Å}})} = 0.3838 \log\left(\frac{L_{2\,\mathrm{keV}}}{L_{2500\,\text{Å}}}\right) \qquad (5)$$

and show in Fig. 3, α_{ox} as a function of L_{UV} for all the sources in Table 1, including also multi-epoch measurements where available. Radio-loud quasars and BAL quasars are also shown with different symbols, and they are then removed from the main correlation.

Radio flux density at 1.4 GHz from FIRST radio survey (Becker et al. 1995) is directly available in the SDSS-DR5 Quasar Catalog, where radio sources are associated with SDSS positions adopting a cross-correlation radius of 2 arcsec (Schneider et al. 2007). In a few cases, additional radio information is taken from the NVSS survey (Condon et al. 1998) and/or from the NASA Extragalactic Database (NED). In total, radio

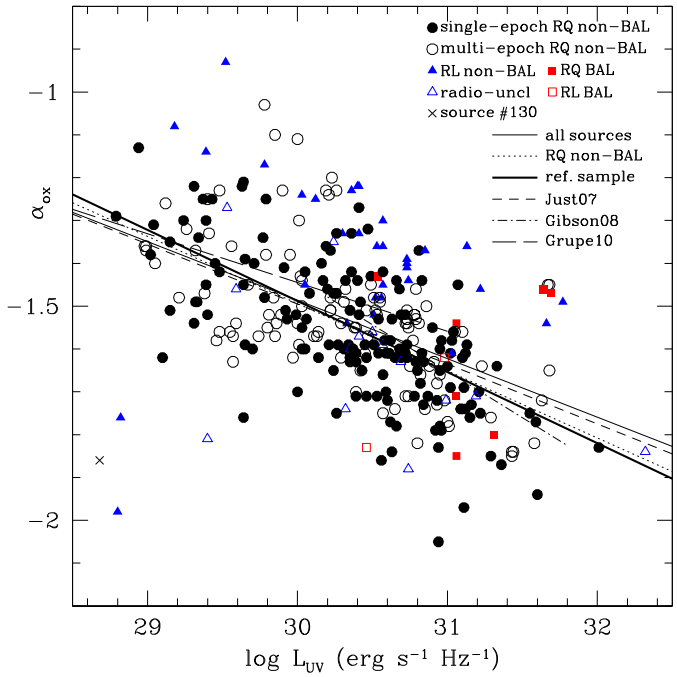

Fig. 3. α_{ox} as a function of the 2500 Å specific luminosity L_{UV}, for all the 315 measurements of the sources in our sample, including multi-epoch measurements. Filled and open circles are, respectively, single-epoch and multi-epoch measurements of radio-quiet, non-BAL AGNs. BAL AGNs are plotted as filled (radio-quiet) and open (radio-loud) squares. Filled triangles represent radio-loud, non-BAL, sources, and open triangles are radio-unclassified sources. The × symbol indicates the anomalously X-ray-weak source #130. Linear fits are represented as thin continuous (all the sources), dotted (radio-quiet non-BAL sources), thick continuous (excluding also source #130). The short-dashed line is the best-fit reported by Just et al. (2007). The dot-dashed, and long-dashed lines are the best-fit relations found by Gibson et al. (2008), and by Grupe et al. (2010), respectively, and are plotted for limited ranges of luminosities, as analysed in the corresponding works.

information is available for 228 sources out of 241 in Table 1. Following Gibson et al. (2008), we assume a radio spectral index $\alpha = -0.8$ to estimate the specific luminosity at 5 GHz. We then calculate the radio-loudness parameter (e.g., Kellermann et al. 1989),

$$R^* = L_\nu(5\,\mathrm{GHz})/L_{2500\,\text{Å}}, \qquad (6)$$

and classify sources with $\log(R^*) \geq 1$ as radio-loud (RL), marking them with $f_{RL} = 1$ in Table 1. Sources without detected radio flux or with $\log(R^*) < 1$ are classified as radio-quiet (RQ) and marked with $f_{RL} = 0$. Sources without radio information from FIRST, NVSS, or NED are marked with $f_{RL} = -1$. Eight sources are present in the Gibson et al. (2008) and Gibson et al. (2009) catalogues as BAL quasars, and are accordingly marked in Table 1 with $f_{BAL} = 1$.

As a first step, we show in Fig. 3 linear least squares fits corresponding to all the available measurements with the same weights, even for multi-epoch sources, as if they were different sources. The thin continuous line is a fit to all the sources, regardless of their radio-loudness and/or BAL characteristics, given by

$$\alpha_{ox} = (-0.137 \pm 0.013) \log L_{UV} + (2.610 \pm 0.401). \qquad (7)$$

A second fit, shown as a dotted line, corresponds to radio-quiet non-BAL sources, which are 193 of 241 in our sample

$$\alpha_{ox} = (-0.157 \pm 0.013) \log L_{UV} + (3.212 \pm 0.386). \qquad (8)$$

[7] With the usual convention of explicit minus sign for the photon index, $P(E) \propto E^{-\Gamma}$ and with the implicit sign adopted by us for the energy index α, the relation between the two indices is $\Gamma = 1 - \alpha$.

Radio-unclassified sources marked in Table 1 with $f_{RL} = -1$, are not included in this fit. Including them would make however a minor difference, as we have verified.

Most of the radio-loud sources in Fig. 3 are located above the fits, as expected, radio-loud quasars being known to have jet-linked X-ray emission components that generally lead to higher X-ray-to-optical ratios than those of radio-quiet quasars (e.g., Worrall et al. 1987).

One source, #130 in Table 1, appears to be very X-ray weak relative to the average correlation, as quantified in Sect. 4.1. This source is discussed further in Sect. 6 and we believe there are reasons to consider it to be anomalous. We then exclude it, so obtaining a reference sample of 192 radio-quiet non-BAL sources, not containing source #130. We indicate with a thick continuous line the corresponding fit

$$\alpha_{ox} = (-0.166 \pm 0.012) \log L_{UV} + (3.489 \pm 0.377). \quad (9)$$

These correlations can be compared with that reported by Gibson et al. (2008), which is shown in Fig. 3 as a dot-dashed line

$$\alpha_{ox} = (-0.217 \pm 0.036) \log L_{UV} + (5.075 \pm 1.118). \quad (10)$$

and with those found by previous authors, usually flatter, as e.g. in Just et al. (2007), whose fit is shown in Fig. 3 as a dashed line:

$$\alpha_{ox} = (-0.140 \pm 0.007) \log L_{UV} + (2.705 \pm 0.212). \quad (11)$$

The analysis of Grupe et al. (2010) is also interesting, because it uses simultaneous X-ray and optical measurements from *Swift*, and has a yet flatter slope

$$\alpha_{ox} = (-0.114 \pm 0.014) \log L_{UV} + (1.177 \pm 0.305). \quad (12)$$

We note that the relations of Gibson et al. (2008) and Grupe et al. (2010) are obtained by means of analyses in limited ranges of UV luminosities and redshifts, respectively of ($30.2 < \log L_{UV} < 31.8$, $1.7 < z < 2.7$) and ($26 < \log L_{UV} < 31$, $z < 0.35$). This suggests a possible dependence of the slope of the $\alpha_{ox} - L_{UV}$ relation on luminosity or redshift or both, and is discussed further in Sect. 4.2.

We now limit ourselves to our reference sample of 192 sources, and show in Fig. 4 (as open circles) the average values of L_{UV} and α_{ox} for 41 multi-epoch sources, together with the corresponding values for 151 single-epoch sources (black dots). Source #45 is a known gravitational lens (Kochanek et al. 1997). Chartas (2000) estimated that its luminosity is amplified by a factor ∼15. We plot this source in Fig. 4 as an open square at the observed luminosity, and deamplified by a factor of 15 as an open circle, connected to the observed point by a dotted line. The parameter α_{ox} is not affected, as gravitational lensing is achromatic.

The best-fit relation to the data in Fig. 4, including source #45 with its deamplified luminosity, is

$$\alpha_{ox} = (-0.178 \pm 0.014) \log L_{UV} + (3.854 \pm 0.420). \quad (13)$$

Separate fits for single-epoch and multi-epoch sources give, respectively, $\alpha_{ox} = (-0.179 \pm 0.016) \log L_{UV} + (3.863 \pm 0.482)$ and $\alpha_{ox} = (-0.171 \pm 0.029) \log L_{UV} + (3.657 \pm 0.877)$.

4.1. Dispersion in α_{ox}

We adopt Eq. (13) as our reference $\alpha_{ox}(L_{UV})$ relation and investigate the dispersion of the sources around it. We therefore define the residuals

$$\Delta\alpha_{ox} = \alpha_{ox} - \alpha_{ox}(L_{UV}). \quad (14)$$

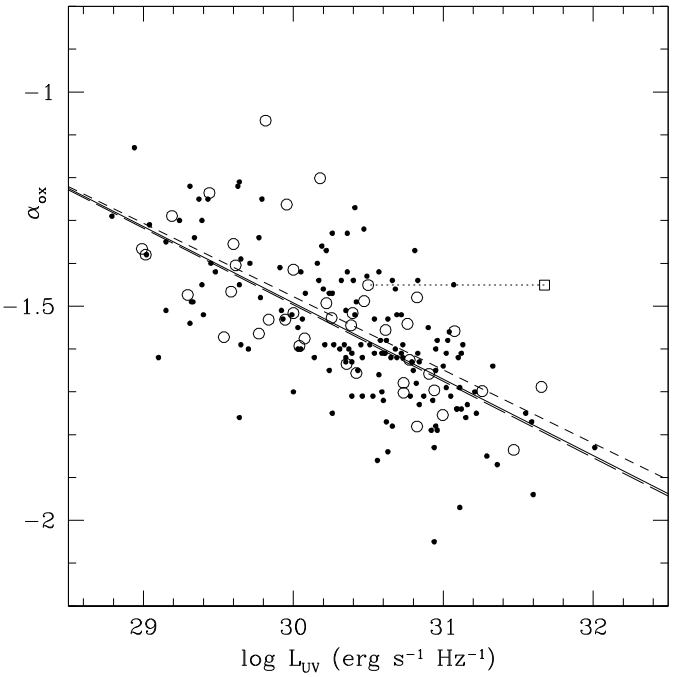

Fig. 4. α_{ox} as a function of the 2500 Å specific luminosity L_{UV}, for the 192 radio-quiet non-BAL sources of the reference sample. Multi-epoch measurements of the same sources are averaged and shown as open circles, while black dots refer to single-epoch sources. Source #45 is a gravitational lens and is shown with both its observed luminosity (as an open square) and its deamplified luminosity (as an open circle). The continuous line shows the least squares fit to the points. Dashed lines show separate fits to the single-epoch (long-dash) and multi-epoch (short-dash) sources.

We show in Fig. 5 the histograms of $\Delta\alpha_{ox}$, using the average values of multi-epoch measurements as in Fig. 4. Contour histogram represents all sources, the filled histogram the reference sample, and source #130 is marked by a cross. The two histograms have standard deviations $\sigma = 0.158$ and $\sigma = 0.122$, respectively. The source #130, with $\Delta\alpha_{ox} = -0.60$, differs by about 5σ from the reference relation, and appears X-ray weaker by a factor of ∼40 than AGNs of the same UV luminosity.

The dispersion in our $\Delta\alpha_{ox}$ distribution is comparable to those obtained by, e.g., Strateva et al. (2005), Just et al. (2007), and Gibson et al. (2008) on the basis of non-simultaneous X-ray and UV data, with values between 0.10 and 0.14. Our result based on simultaneous data eliminates a possible cause of dispersion due to "artificial α_{ox} variability". The dispersion is not lower than previous non-simultaneous estimates, thus it is probably caused by other factors affecting the X-ray/UV ratio. These could include: (i) "intra-source dispersion", caused by "intrinsic α_{ox} variability", i.e., true temporal change in the X-ray/UV ratio for individual sources, and/or (ii) "inter-source dispersion", due to intrinsic differences in the average α_{ox} values from source to source, perhaps related to different conditions in the emitting regions.

4.2. Dependence on z and L

To estimate the possible dependence of α_{ox} on redshift, we perform a partial correlation analysis, correlating α_{ox} with L_{UV}, with account for the effect of z, and correlating α_{ox} with z, taking account of the effect of L_{UV}. For our reference sample of 192 radio-quiet, non-BAL, sources, we find a Pearson

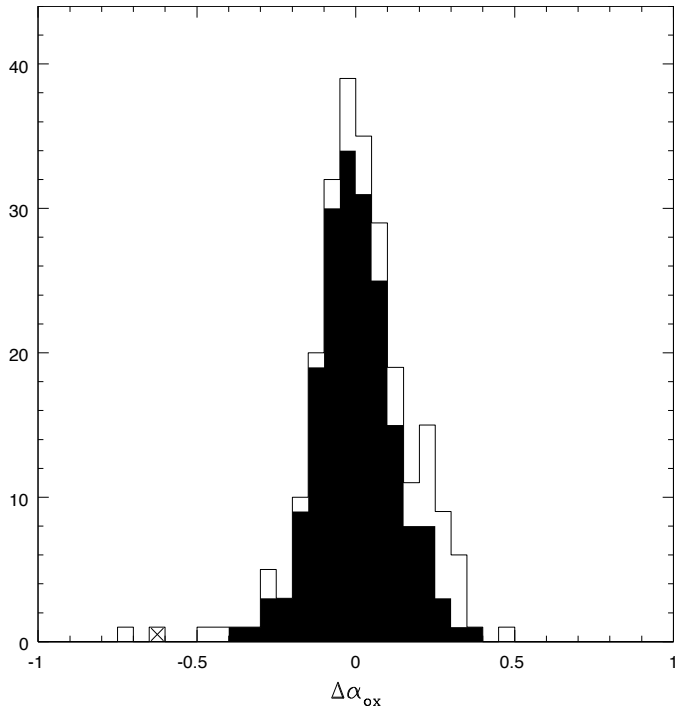

Fig. 5. Histograms of the residuals $\Delta\alpha_{ox}$ (Eq. (14)) for all the sources (contour histogram), and for the reference sample (filled histogram). Source #130 is marked by a cross. Dispersions for the two samples are $\sigma = 0.158$ and $\sigma = 0.122$, respectively.

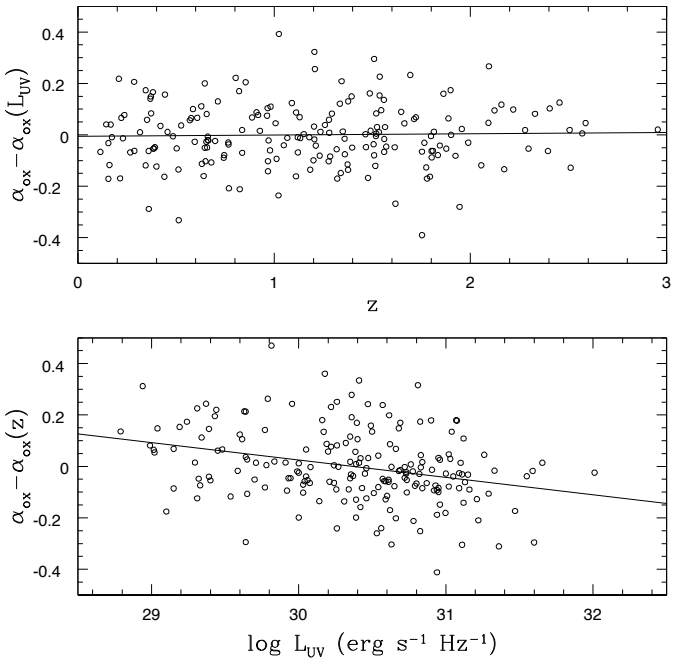

Fig. 6. *Upper panel*: residuals $\alpha_{ox} - \alpha_{ox}(L_{UV})$, as a function of z. *Lower panel*: residuals $\alpha_{ox} - \alpha_{ox}(z)$ as a function of $\log L_{UV}$.

partial correlation coefficient $r_{\alpha L,z} = -0.51$, with a probability $P(>r) = 1.3 \times 10^{-12}$ for the null hypothesis that α_{ox} and L_{UV} are uncorrelated. The other partial correlation coefficient is $r_{\alpha z,L} = 0.05$ with $P(>r) = 0.52$, which implies that there is no evidence of a correlation with z.

Our results agree with previous studies (Avni & Tananbaum 1986; Strateva et al. 2005; Steffen et al. 2006; Just et al. 2007), which also found no evidence of a dependence of α_{ox} on redshift (see however Kelly et al. 2007).

In the upper panel of Fig. 6, we plot the residuals $\alpha_{ox} - \alpha_{ox}(L_{UV})$, Eq. (14), as a function of z, which show no correlation ($r = 0.027$, $P(>r) = 0.703$, $\Delta\alpha_{ox} = (0.005 \pm 0.014)z + (-0.006 \pm 0.018)$). In the lower panel, we plot the residuals $\alpha_{ox} - \alpha_{ox}(z)$ as a function of $\log L_{UV}$, after computing the average $\alpha_{ox} - z$ relation, $\alpha_{ox}(z) = (-0.139 \pm 0.016)z + (-1.394 \pm 0.022)$. These residuals clearly decrease with luminosity ($r = -0.305$, $P(>r) = 2.4 \times 10^{-5}$, $\Delta\alpha_{ox} = (-0.067 \pm 0.015) \log L_{UV} + (2.050 \pm 0.465)$). Similar results were obtained by Steffen et al. (2006). These results suggest that the dependence of α_{ox} on z is induced by the intrinsic dependence on L_{UV} through the $L_{UV} - z$ correlation.

The slope of the $\alpha_{ox} - L_{UV}$ relation, according to the fits by Gibson et al. (2008) and Grupe et al. (2010), shown in Fig. 3 with the results of Just et al. (2007) and ourselves, may be flatter at lower luminosity and/or redshift. We divide our reference sample into two equally populated subsamples, $\log L_{UV} \lessgtr 30.43$, finding $\alpha_{ox} = (-0.137 \pm 0.029) \log L_{UV} + (2.639 \pm 0.878)$ for the low luminosity sources, and $\alpha_{ox} = (-0.193 \pm 0.038) \log L_{UV} + (4.319 \pm 1.182)$ for the high luminosity ones, while for the entire sample Eq. (13) is valid. A Student's-t test applied to the low-L_{UV} and high-L_{UV} subsamples gives a 12% probability that they are drawn from the same parent distribution. A similar result was found by Steffen et al. (2006).

We similarly divide our sample into two redshift subsamples, $z \lessgtr 1.2$, finding $\alpha_{ox} = (-0.166 \pm 0.022) \log L_{UV} + (3.491 \pm 0.650)$ for the low z sources, and $\alpha_{ox} = (-0.225 \pm 0.033) \log L_{UV} + (5.305 \pm 1.015)$ for the high z sources. Application of the Student's-t test gives in this case a 7% probability that low-z and high-z subsamples are drawn from the same parent distribution.

This suggests that the slope of the $\alpha_{ox} - L_{UV}$ relation may be L_{UV}- and/or z-dependent. However, the apparent dependence on z can be an artifact of a true dependence on L_{UV}, or vice versa. A sample of sources evenly distributed in the $L - z$ plane is required to distinguish these dependences.

5. Multi-epoch data

We show in Fig. 7 the tracks of individual sources in the $\alpha_{ox} - L_{UV}$ plane, for the reference sample. Only 41 of 192 sources have multi-epoch information, and most of them exhibit small variations. Some sources (#73, #168) have strong variations in both α_{ox} and L_{UV}, but nearly parallel to the average $\alpha_{ox} - L_{UV}$ relation, therefore not contributing appreciably to the dispersion in $\Delta\alpha_{ox}$. A few sources (e.g., #90, #157, #225) have appreciable or strong variations perpendicular to the average relation, possibly contributing to the overall dispersion. Figure 8 shows a histogram of the individual dispersions in $\Delta\alpha_{ox}$ for these 41 sources.

Most sources have data at only 2 epochs, and only 9 sources have more epochs, up to 9. The individual variations occur on different timescales, from hrs to yrs, and cannot be directly compared with each other. It is however possible to build an ensemble structure function (SF) to describe the variability in a given quantity $A(t)$ for different rest-frame time-lags τ. We define it as in di Clemente et al. (1996)

$$SF(\tau) = \frac{\pi}{2}\langle|A(t+\tau) - A(t)|\rangle. \quad (15)$$

The factor $\pi/2$ is introduced to measure SF in units of standard deviations, and the angular brackets indicate the ensemble average over appropriate bins of time lag. The function $A(t)$ is usually a flux or luminosity in a given spectral band, or its logarithm.

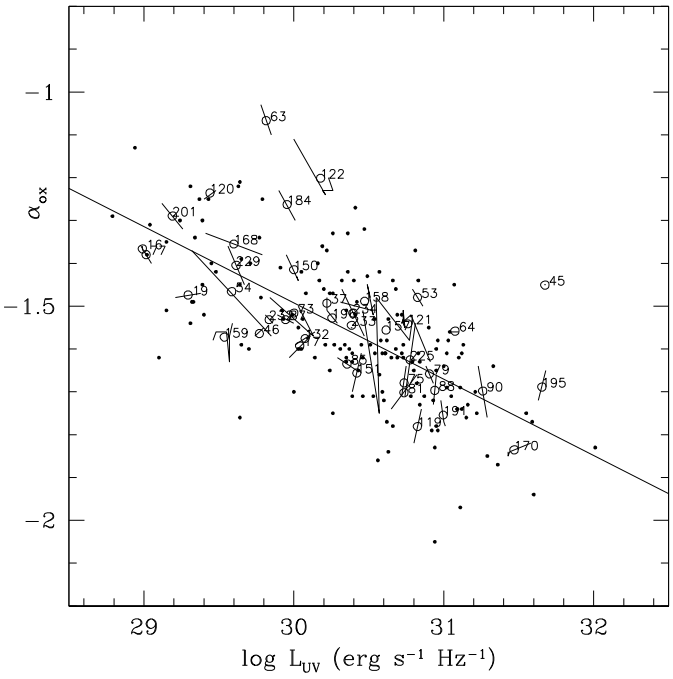

Fig. 7. behaviour of individual radio-quiet non-BAL sources in the plane $\alpha_{ox} - L_{UV}$. Connected segments show the tracks of multi-epoch sources, while open circles represent the average values of the same sources, which are labeled with their serial numbers as in Table 1. Small dots refer to single-epoch sources. The straight line is the adopted $\alpha_{ox} - L_{UV}$ relation, Eq. (13).

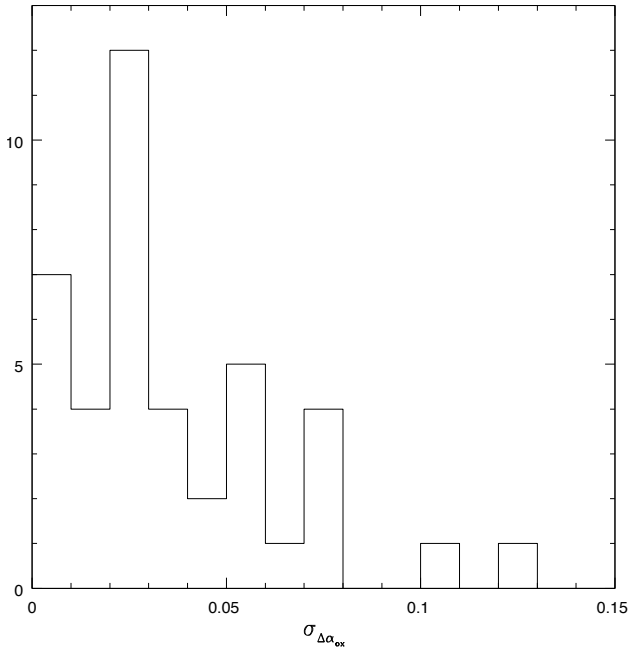

Fig. 8. Histogram of the individual dispersions of $\Delta\alpha_{ox}$ for the 41 radio-quiet non-BAL sources with multi-epoch information.

Here, we apply the definition of Eq. (15) to both $\alpha_{ox}(t)$ and the residuals $\Delta\alpha_{ox}(t)$. The result is illustrated in Fig. 9 for both functions. There is a clear increase in both SFs, which reach average variations of up to ∼0.07 at ∼1 yr rest-frame. Unfortunately, the sampling is quite irregular, and most sources contribute with single points (corresponding to 2 epochs), while the few sources with more epochs have a greater weight in the ensemble statistic. To check whether the increase in SFs may be due to a

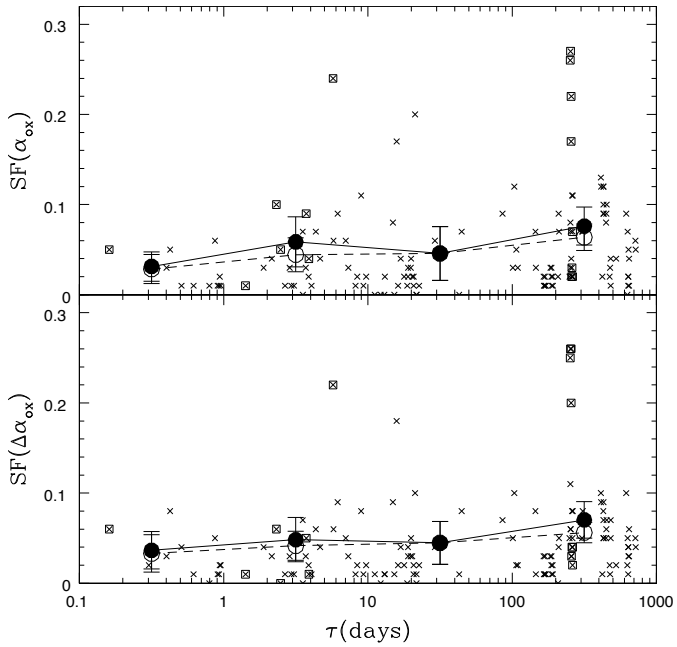

Fig. 9. Rest-frame structure function of $\alpha_{ox}(t)$ (*upper panel*) and the residuals $\Delta\alpha_{ox}(t)$ (*lower panel*) for the 41 radio-quiet non-BAL sources with multi-epoch data. The crosses represent the contributions of the variations in individual sources. All the points marked by open squares refer to the variable source #157. The filled circles connected by continuous lines represent the ensemble structure function for the set of 41 sources, in bins of $\Delta \log \tau = 1$. The open circles connected by dashed lines correspond to the remaining set of 40 sources, after removing source #157.

single highly variable source, we compute new SFs by removing source #157, which also has a relatively high number of epochs ($n = 6$ epochs, therefore contributing $n(n-1)/2 = 15$ SF points), and find in this case a slightly smaller (but still relevant) increase (∼0.06 at ∼1 yr).

These values can be compared with the dispersion in the residuals shown in Fig. 5, which is $\sigma = 0.122$ for the reference sample. We note that the ensemble variability of $\Delta\alpha_{ox}$ was computed for only 41 multi-epoch sources, while the filled histogram shown in Fig. 5 also includes 151 single-epoch sources. We then checked whether the dispersions in the residuals for the single-epoch and multi-epoch subsamples are similar, being $\sigma = 0.122$ and $\sigma = 0.119$, respectively.

It then appears that variability in α_{ox} could account for a large part of the observed dispersion around the average $\alpha_{ox} - L_{UV}$ correlation. It is reasonable to expect that sources measured at single-epochs have temporal behaviours similar to those described by the SFs of Fig. 9, and that the variations in individual sources during their lifetime are similar to the variations measured from source to source at random epochs. However, the average temporal values of individual sources may differ, and "inter-source dispersion" may be present, in addition to "intra-source dispersion" (see Sect. 4.1). Assuming that other factors contributing to the dispersion can be neglected, the overall variance would then be:

$$\sigma^2 = \sigma^2_{\rm intra-source} + \sigma^2_{\rm inter-source}. \quad (16)$$

Our structure function analysis infers a value of 0.07 for the intra-source dispersion at 1 yr (or 0.06 if we remove the highly variable source #157), while the total dispersion in the residuals shown in Fig. 5 is $\sigma \sim 0.12$. This would indicate a ∼30%

contribution of intra-source dispersion to the total variance σ^2. However, the SF may increase further at longer time delays, so that the contribution of intra-source dispersion would be higher, while that of inter-source dispersion would be constrained toward lower values.

Other factors may affect the dispersion, for example: (i) errors in the extrapolations of UV and X-ray luminosities; (ii) differences in galactic absorption; (iii) spurious inclusion of unknown BAL sources. From Fig. 2, it appears that a few sources have SEDs with anomalous slopes, and extrapolations with the average SED by Richards et al. (2006) infer in these cases poor luminosity estimates; however, this applies only to a small fraction of the sample. For X-rays, we adopted $\Gamma = 1.7$ to be consistent with the fluxes catalogued in the XMMSSC; a distribution of Γ values would introduce an extra dispersion. All these factors would probably contribute an additional term in Eq. (16). This would constrain more tightly the contribution of the inter-source dispersion, therefore increasing the relative weight of variability and intra-source dispersion.

A finer sampling of the SF and a homogeneous weight of the individual sources are however needed to quantify more definitely the contribution of variability, and which fraction has yet to be explained by other factors. Simultaneous UV and X-ray observations for a homogeneous sample of sources no greater than our own would be sufficient, assuming that each source is observed at ∼10 epochs, spanning a monitoring time of a few years.

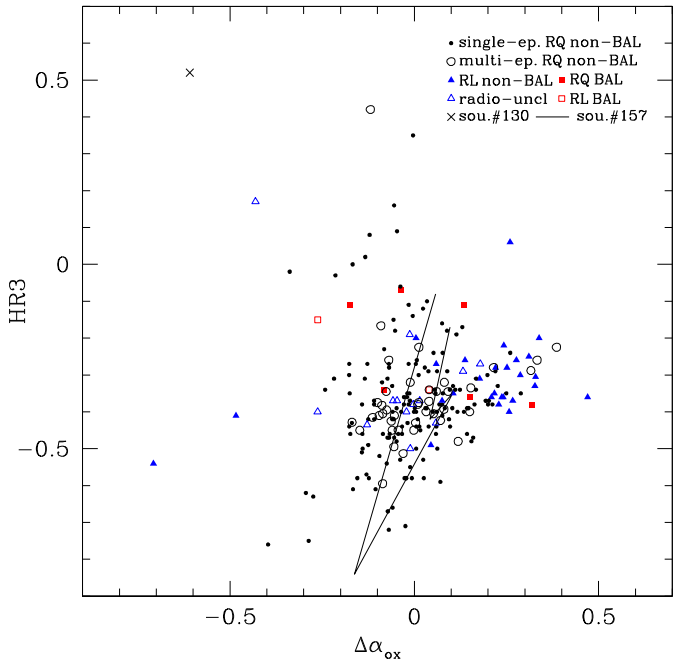

Fig. 10. Plot of the sources of Table 1 in the plane $\Delta\alpha_{ox} - HR3$. Symbols as in Fig. 3. Sources with multi-epoch data are represented by their average values, except source #157, whose strong variations are also shown by the connected segments.

6. Peculiar sources

6.1. 2XMM J112611.6+425245

We computed the X-ray luminosity and the α_{ox} spectral index starting from the X-ray flux in the 2−4.5 keV band (*XMM-Newton* band 4), as described in Sect. 3. Since 2XMM J112611.6+425245 (source #130) is X-ray weak by a factor ∼40, we analysed the X-ray information in the various *XMM-Newton* bands, available in the XMMSSC catalogue, and found this source to be even weaker in the softer 1−2 keV band (band 3), with a very high hardness ratio between the two bands, $HR3 = (CR4 - CR3)/(CR4 + CR3) = 0.52$, $CR3$ and $CR4$ being the count rates in the two bands. We then plot the sources of Table 1 in the plane $\Delta\alpha_{ox} - HR3$, to see whether X-ray weak sources are in some way related to particular values of the X-ray hardness ratio. This is shown in Fig. 10, where it can be seen that most sources are concentrated in a region with "standard" values around $\Delta\alpha_{ox} = 0$ and $HR3 \simeq -0.4$, while a few sources are located at greater distances, along tails in various directions. Source #130, indicated by a × sign in the figure, is the most distant, and very X-ray weak and very hard.

Hu et al. (2008) report this source (which has a redshift $z = 0.156$) in their study of the FeII emission in quasars, where it is shown that systematic inflow velocities of FeII emitting clouds are inversely correlated with Eddington ratios. The source 2XMM J112611.6+425245 has one of the highest measured inflow velocities, $v_{Fe} \sim 1700$ km s^{-1}. Ferland et al. (2009) argue about the high column densities, $N_H \sim 10^{22}$–10^{23} cm^{-2}, necessary to account for the inflows in this class of quasars, and about the possibility that either UV or X-ray absorption are associated with the infalling component.

The source 2XMM J112611.6+425245 also has a high $HR4 = (CR5 - CR4)/(CR5 + CR4) = 0.63$, $CR5$ being the count rate in the 4.5−12 keV energy band. High values of $HR3$ and $HR4$ are used by Noguchi et al. (2009) to select, on the basis of a modelling of the direct and scattered emission, a sample of AGNs hidden by geometrically thick tori. The hardness ratios of this source imply that it is a good candidate for that class of AGNs.

6.2. 2XMM J123622.9+621526

Source #157 is one of those with the greatest variance in $\Delta\alpha_{ox}$. It exhibits even more extraordinary variations in $HR3$, which are shown in Fig. 10 by a broken line. It is in the Chandra Deep Field North, and its X-ray spectrum, analysed by Bauer et al. (2004), classifies it as an unobscured quasar. While its UV luminosity has remained nearly constant, its $\Delta\alpha_{ox}$ and $HR3$ have varied by 0.22 and 0.76, respectively, between epochs 5 and 6 in Table 1, which differ by 20 days in the observed frame, i.e., less than a week in the rest-frame at the redshift $z = 2.597$.

7. Discussion

The behaviour of α_{ox}, i.e., its dependence on luminosity and redshift, its dispersion and variability, are to be considered as symptoms of the relation between disk and corona emissions and their variabilities.

It is generally believed that variable X-ray irradiation can drive optical variations by means of variable heating of the internal parts of the disk on relatively short timescales, days to weeks, while intrinsic disk instabilities in the outer parts of the disk dominate on longer timescales, months to years, propagating inwards and modulating X-ray variations in terms of Compton up-scattering in the corona (Czerny 2004; Arévalo 2006, 2009; Papadakis et al. 2008; McHardy 2010).

The structure functions of the light curves increase on long timescales both in the optical (e.g., di Clemente et al. 1996; Vanden Berk et al. 2004; Bauer et al. 2009) and X-rays (e.g.,

Fiore et al. 1998, Vagnetti et al., in prep.). This, however, does not imply that the α_{ox} SF also increases with time lag. Larger changes (on long time lags) in both X-ray and UV fluxes may occur without changes in the spectral shape (i.e., with constant α_{ox}). Our results shown in Fig. 9 indicate that this is not the case, i.e., that slope changes are indeed larger on longer timescales.

Moreover, it is evident from Fig. 9 that most of the dispersion about the $\alpha_{ox} - L_{UV}$ relation is due, in the present sample, to variations on timescales from months to years, which are associated with optically driven variations, according to the general belief.

The α_{ox} structure function does not distinguish between the hardening or softening of the optical to X-ray spectrum during brightening. This is instead described by the spectral variability parameter $\beta = \partial\alpha/\partial \log F$ (Trevese et al. 2001; Trevese & Vagnetti 2002), which can be adapted to the optical-X-ray case to become

$$\beta_{ox} = \frac{\delta\alpha_{ox}}{\delta \log L_{UV}}, \quad (17)$$

where β_{ox} is the slope of the correlated variations $\delta\alpha_{ox}$ and δL_{UV}, and describes whether a source hardens when it brightens or vice versa, i.e., if the X-ray luminosity increases more than the optical or less. For example, single source variations parallel to the α_{ox} anticorrelation have a negative β_{ox}, while variations perpendicular to the correlation have $\beta_{ox} > 0$. Both of these behaviours can be seen in Fig. 7.

Of course, the different behaviour of the sources in the $\alpha_{ox} - L_{UV}$ plane may correspond to a different time sampling. Constraining physical models of the primary variability source and disk-corona coupling would require the analysis of β_{ox} as a function of the time lag. This analysis does not look feasible, i.e., to have statistical reliability, with the present sparse sampling. We can propose more conventional scenarios and note that since most of the variability, in the present sample, occurs on long ($\sim$ 1 year) timescale, it is presumably associated with optically driven variations. Considering all the measured variations $\delta\alpha_{ox}$ and δL_{UV}, we obtain the "ensemble" average $\langle\beta_{ox}\rangle = -0.240$. The negative sign implies that, on average, a spectral steepening occurs in the brighter phase. This is, in fact, consistent with larger variations in the *UV* band, driving the X-ray variability. The value of $\langle\beta_{ox}\rangle$ can be compared with the average slope of the $\alpha_{ox} - L_{UV}$ relation, Eq. (13), indicating that the UV excess in the brighter phase (steepening) is larger than the average UV excess in bright objects respect to faint ones.

Finally we emphasise that, despite its limitations, the present analysis illustrates the feasibility of an ensemble analysis of the $\alpha_{ox} - L_{UV}$ correlation, e.g., by considering the β parameter as a function of time lag. What is presently missing is an adequate simultaneous X-ray-UV sampling, at relatively short time lags, of a statistical AGN sample. An ensemble analysis may provide important constraints even when the total number of observations does not allow us to carry out a cross-correlation analysis of X-ray and UV variations of individual sources.

We summarise our main results as follows:

- we have studied the $\alpha_{ox} - L_{UV}$ anticorrelation with simultaneous data extracted from the *XMM-Newton* Serendipitous Source catalogues;
- we confirm the anticorrelation, with a slope (-0.178) slightly steeper w.r.t. Just et al. (2007);
- we do not find evidence for a dependence of α_{ox} on redshift, in agreement with previous authors (e.g. Avni & Tananbaum 1986; Strateva et al. 2005; Steffen et al. 2006; Just et al. 2007);
- there appears to be a flatter slope to the anticorrelation at low luminosities and low redshifts, in agreement with previous results by Steffen et al. (2006);
- the dispersion in our simultaneous data ($\sigma \sim 0.12$) is not significantly smaller w.r.t. previous non-simultaneous studies (Strateva et al. 2005; Just et al. 2007; Gibson et al. 2008), indicating that "artificial α_{ox} variability" introduced by non-simultaneity is not the main cause of dispersion;
- "intrinsic α_{ox} variability", i.e., true variability in the X-ray to optical ratio, is important, and accounts for $\sim$30% of the total variance, or more;
- "inter-source dispersion", due to intrinsic differences in the average α_{ox} values from source to source, is also important;
- the dispersion introduced by variability is mostly caused by the long timescale variations, which are expected to be dominated by the optical variations; the average spectral softening observed in the bright phase is consistent with this view;
- distinguishing the trends produced by optical or X-ray variations may be achievable using the ensemble analysis of the spectral variability parameter β_{ox} as a function of time lag; crucial information would be provided by wide field simultaneous UV and X-ray observations with relatively short (days-weeks) time lags.

Acknowledgements. We thank P. Giommi and A. Paggi for useful discussions. This research has made use of the *XMM-Newton* Serendipitous Source Catalogue, which is a collaborative project involving the whole Science Survey Center Consortium. This research has made use of the XMM-OM Serendipitous Ultra-violet Source Survey (XMMOMSUSS), which has been created at the University College London's (UCL's) Mullard Space Science Laboratory (MSSL) on behalf of ESA and is a partner resource to the 2XMM serendipitous X-ray source catalogue. Funding for the SDSS and SDSS-II has been provided by the Alfred P. Sloan Foundation, the Participating Institutions, the National Science Foundation, the U.S. Department of Energy, the National Aeronautics and Space Administration, the Japanese Monbukagakusho, the Max Planck Society, and the Higher Education Funding Council for England. The SDSS Web Site is http://www.sdss.org/. This research has made use of the NASA/IPAC Extragalactic Database (NED), which is operated by the Jet Propulsion Laboratory, California Institute of Technology, under contract with the National Aeronautics and Space Administration. This work makes use of EURO-VO software, tools or services. The EURO-VO has been funded by the European Commission through contract numbers RI031675 (DCA) and 011892 (VO-TECH) under the 6th Framework Programme and contract number 212104 (AIDA) under the 7th Framework Programme. S.T. acknowledges financial support through Grant ASI I/088/06/0.

References

Arévalo, P. 2006, in VI Microquasar Workshop: Microquasars and Beyond, PoS(MQW6)032
Arévalo, P. 2009, in ed. W. Wang, Z. Yang, Z. Luo, & Z. Chen, ASP Conf. Ser., 408, 296
Avni, Y., & Tananbaum, H. 1986, ApJ, 305, 83
Bauer, A., Baltay, C., Coppi, P., et al. 2009, ApJ, 696, 1241
Bauer, F. E., Vignali, C., Alexander, D. M., et al. 2004, Adv. Space Res., 34, 2555
Becker, R. H., White, R. L., & Helfand, D. J. 1995, ApJ, 450, 559
Brandt, W. N., Laor, A., & Wills, B. J. 2000, ApJ, 528, 637
Chartas, G. 2000, ApJ, 531, 81
Condon, J. J., Cotton, W. D., Greisen, E. W., et al. 1998, AJ, 115, 1693
Czerny, B. 2004, The role of an accretion disk in AGN variability [arXiv:astro-ph/0409254]
di Clemente, A., Giallongo, E., Natali, G., Trevese, D., & Vagnetti, F. 1996, ApJ, 463, 466
Ferland, G. J., Hu, C., Wang, J., et al. 2009, ApJ, 707, L82
Fiore, F., Laor, A., Elvis, M., Nicastro, F., & Giallongo, E. 1998, ApJ, 503, 607

Giallongo, E., Trevese, D., & Vagnetti, F. 1991, ApJ, 377, 345
Gibson, R. R., Brandt, W. N., & Schneider, D. P. 2008, ApJ, 685, 773
Gibson, R. R., Jiang, L., Brandt, W. N., et al. 2009, ApJ, 692, 758
Grupe, D., Komossa, S., Leighly, K. M., & Page, K. L. 2010, ApJS, 187, 64
Hu, C., Wang, J.-M., Ho, L. C., et al. 2008, ApJ, 687, 78
Just, D. W., Brandt, W. N., Shemmer, O., et al. 2007, ApJ, 665, 1004
Kellermann, K. I., Sramek, R., Schmidt, M., Shaffer, D. B., & Green, R. 1989, AJ, 98, 1195
Kelly, B. C., Bechtold, J., Siemiginowska, A., Aldcroft, T., & Sobolewska, M. 2007, ApJ, 657, 116
Kochanek, C. S., Falco, E. E., Schild, R., et al. 1997, ApJ, 479, 678
La Franca, F., Franceschini, A., Cristiani, S., & Vio, R. 1995, A&A, 299, 19
Leighly, K. M., Halpern, J. P., Jenkins, E. B., et al. 2007, ApJ, 663, 103
Markowitz, A., Edelson, R., & Vaughan, S. 2003, ApJ, 598, 935
Mason, K. O., Breeveld, A., Much, R., et al. 2001, A&A, 365, L36
McHardy, I. 2010, in Lecture Notes in Physics, The Jet Paradigm, ed. T. Belloni (Berlin: Springer Verlag), 794, 203
Noguchi, K., Terashima, Y., & Awaki, H. 2009, ApJ, 705, 454
Papadakis, I. E., Chatzopoulos, E., Athanasiadis, D., Markowitz, A., & Georgantopoulos, I. 2008, A&A, 487, 475
Richards, G. T., Lacy, M., Storrie-Lombardi, L. J., et al. 2006, ApJS, 166, 470
Schneider, D. P., Hall, P. B., Richards, G. T., et al. 2007, AJ, 134, 102
Smith, R., & Vaughan, S. 2007, MNRAS, 375, 1479
Steffen, A. T., Strateva, I., Brandt, W. N., et al. 2006, AJ, 131, 2826
Strateva, I. V., Brandt, W. N., Schneider, D. P., Vanden Berk, D. G., & Vignali, C. 2005, AJ, 130, 387
Trevese, D., & Vagnetti, F. 2002, ApJ, 564, 624
Trevese, D., Kron, R. G., & Bunone, A. 2001, ApJ, 551, 103
Vanden Berk, D. E., Wilhite, B. C., Kron, R. G., et al. 2004, ApJ, 601, 692
Vignali, C., Brandt, W. N., & Schneider, D. P. 2003, AJ, 125, 433
Watson, M. G., Schröder, A. C., Fyfe, D., et al. 2009, A&A, 493, 339
Worrall, D. M., Tananbaum, H., Giommi, P., & Zamorani, G. 1987, ApJ, 313, 596
Yuan, W., Siebert, J., & Brinkmann, W. 1998, A&A, 334, 498

Pages 11 to 16 are available in the electronic edition of the journal at http://www.aanda.org

Table 1. The sources.

N_{sou} (1)	N_{epo} (2)	Source (3)	Epoch (4)	z (5)	f_{RL}[a] (6)	f_{BAL}[b] (7)	$\log L_{UV}$ (8)	$\log L_X$ (9)	α_{ox} (10)	$\Delta\alpha_{ox}$ (11)	$HR3$ (12)
1		2XMM J003922.3+005951	53 365.828	1.989	0	0	31.05	26.58	−1.71	−0.04	−0.46
2		2XMM J010647.9+004628	52 835.359	1.877	0	0	31.09	26.55	−1.74	−0.06	−0.42
3		2XMM J011902.9−005633	52 831.922	1.614	0	0	30.39	26.20	−1.61	−0.05	−0.47
4		2XMM J014251.7+133352	51 916.445	1.075	−1	0	30.24	26.71	−1.35	0.18	−0.27
5		2XMM J014814.0+140853	52 662.000	0.373	−1	0	29.53	26.22	−1.27	0.13	−0.29
6		2XMM J015254.0+010435	52 276.062	0.570	0	0	29.24	25.84	−1.30	0.05	−0.40
7		2XMM J015258.6+010507	52 276.062	0.647	0	0	29.93	25.94	−1.53	−0.06	−0.15
8		2XMM J015704.1−005656	53 565.277	1.779	0	0	30.94	26.16	−1.83	−0.18	−0.44
9		2XMM J015733.8−004823	53 565.277	1.545	0	0	31.03	26.92	−1.58	0.09	−0.29
10		2XMM J020118.6−091936	53 023.926	0.661	0	0	30.51	26.35	−1.59	−0.01	−0.35
11		2XMM J021100.8−095138	53 016.961	0.767	0	0	30.34	26.21	−1.59	−0.04	−0.46
12		2XMM J023057.3−010033	53 398.395	0.650	0	0	30.14	25.93	−1.62	−0.11	−0.38
13		2XMM J024040.8−081309	53 747.141	1.844	0	0	30.82	26.43	−1.68	−0.05	−0.39
14		2XMM J024055.8−081952	53 747.141	1.802	0	0	30.87	26.40	−1.71	−0.07	−0.27
15		2XMM J024105.8−081153	53 747.141	0.979	0	0	30.21	26.06	−1.59	−0.07	−0.46
16	1	2XMM J024207.2+000038	51 754.270	0.384	0	0	28.99	25.43	−1.37	−0.06	−0.44
16	2	2XMM J024207.2+000038	51 755.121	0.384	0	0	28.99	25.43	−1.36	−0.05	−0.46
17	1	2XMM J024215.0−000209	51 754.270	1.012	0	0	29.97	25.75	−1.62	−0.14	−0.58
17	2	2XMM J024215.0−000209	51 755.121	1.012	0	0	30.11	26.03	−1.57	−0.06	−0.17
18		2XMM J024304.6+000005	51 754.270	1.995	0	1	31.06	27.04	−1.54	0.13	−0.11
19	1	2XMM J024308.1−000126	51 754.270	0.679	0	0	29.21	25.35	−1.48	−0.13	−0.52
19	2	2XMM J024308.1−000126	51 755.121	0.679	0	0	29.38	25.56	−1.47	−0.09	−0.31
20		2XMM J025301.5−011148	52 836.367	0.769	0	0	30.00	25.57	−1.70	−0.21	−0.03
21		2XMM J030357.4−010906	53 785.020	1.520	0	0	30.96	26.85	−1.58	0.08	−0.24
22		2XMM J030627.5−001816	53 212.285	1.538	0	0	30.36	26.88	−1.33	0.22	−0.29
23		2XMM J030639.6+000725	52 681.762	2.172	0	0	30.92	26.26	−1.79	−0.14	−0.50
24		2XMM J030641.7+000109	52 681.762	1.397	0	0	30.27	26.13	−1.59	−0.06	−0.42
25		2XMM J030707.3−000424	52 681.762	0.664	0	0	29.64	25.87	−1.45	−0.03	−0.38
26		2XMM J033810.1+002324	52 327.367	1.120	−1	0	30.50	26.44	−1.56	0.02	−0.37
27		2XMM J033852.8+001905	52 327.367	0.459	−1	0	29.40	24.69	−1.81	−0.43	0.17
28		2XMM J034131.1−011405	53 026.754	1.791	−1	0	30.74	25.85	−1.88	−0.26	−0.40
29		2XMM J073601.4+434455	52 205.023	1.814	0	0	30.84	26.59	−1.63	0.01	−0.44
30		2XMM J074110.6+311200	52 018.582	0.631	1	0	30.74	26.99	−1.44	0.18	−0.31
31		2XMM J074222.3+494147	52 025.754	0.927	0	0	30.58	26.45	−1.58	0.01	−0.42
32		2XMM J080711.0+390419	52 764.121	0.369	0	0	29.43	26.17	−1.25	0.13	−0.40
33		2XMM J081014.5+280337	52 552.309	0.821	0	0	30.66	26.91	−1.44	0.16	−0.38
34		2XMM J081030.2+281326	52 552.309	0.887	0	0	30.20	26.39	−1.46	0.06	−0.40
35		2XMM J081108.6+280500	52 552.309	1.560	0	0	30.57	26.25	−1.66	−0.07	−0.31
36		2XMM J082257.6+404149	53 464.184	0.865	1	0	30.12	26.87	−1.25	0.26	−0.40
37	1	2XMM J084905.0+445714	52 197.344	1.259	0	0	30.22	26.37	−1.48	0.05	−0.35
37	2	2XMM J084905.0+445714	52 203.820	1.259	0	0	30.22	26.29	−1.51	0.02	−0.45
38		2XMM J085522.9+375425	53 653.344	2.296	0	0	31.09	26.56	−1.74	−0.06	−0.33
39		2XMM J085551.1+375752	53 653.344	1.929	0	1	31.31	26.62	−1.80	−0.08	−0.34
40		2XMM J085609.4+374928	53 653.344	2.570	0	0	31.59	26.96	−1.77	−0.00	−0.40
41		2XMM J085724.0+090349	52 743.902	1.049	0	0	31.22	26.65	−1.75	−0.05	0.09
42		2XMM J085808.9+274522	53 469.824	1.090	0	0	30.40	26.65	−1.44	0.12	−0.40
43		2XMM J090029.0+390145	53 108.977	0.964	0	0	30.63	26.65	−1.53	0.07	−0.38
44		2XMM J091029.0+542719	53 457.977	0.526	0	0	30.08	26.25	−1.47	0.03	−0.39
45	1	2XMM J091301.0+525929	52 746.621	1.377	0	0	31.67	27.90	−1.45	0.33	−0.25
45	2	2XMM J091301.0+525929	52 777.559	1.377	0	0	31.68	27.89	−1.45	0.34	−0.27
46	1	2XMM J091302.8+530322	52 746.621	0.631	0	0	29.80	25.75	−1.55	−0.10	0.41
46	2	2XMM J091302.8+530322	52 777.559	0.631	0	0	29.74	25.64	−1.57	−0.13	0.43
47		2XMM J091345.5+405629	52 756.375	0.442	1	0	29.52	27.11	−0.93	0.47	−0.36
48		2XMM J091528.7+441633	53 289.238	1.489	1	0	31.22	27.42	−1.46	0.24	−0.22
49		2XMM J091617.4+303038	52 751.641	0.215	0	0	29.15	25.22	−1.51	−0.18	−0.35
50		2XMM J092138.4+301546	52 752.086	1.590	0	1	31.06	26.24	−1.85	−0.18	−0.11
51		2XMM J092238.3+512120	53 651.457	1.753	0	0	30.35	26.12	−1.62	−0.07	−0.67
52		2XMM J092246.9+512037	53 651.457	0.160	0	0	29.33	25.44	−1.49	−0.12	−0.58
53	1	2XMM J093359.2+551550	52 374.898	1.863	0	0	30.79	26.99	−1.46	0.17	−0.31

Table 1. continued.

N_{sou} (1)	N_{epo} (2)	Source (3)	Epoch (4)	z (5)	f_{RL}[a] (6)	f_{BAL}[b] (7)	log L_{UV} (8)	log L_X (9)	α_{ox} (10)	$\Delta\alpha_{ox}$ (11)	$HR3$ (12)
53	2	2XMM J093359.2+551550	52 381.078	1.863	0	0	30.86	26.95	−1.50	0.14	−0.36
54	1	2XMM J094404.3+480647	53 292.855	0.392	0	0	29.85	25.78	−1.57	−0.11	−0.35
54	2	2XMM J094404.3+480647	53 322.395	0.392	0	0	29.32	25.75	−1.37	−0.01	−0.47
55		2XMM J094409.6+480813	53 322.395	1.111	0	0	29.70	25.53	−1.60	−0.17	−0.00
56		2XMM J094437.9+035936	53 143.621	1.335	0	0	30.16	26.50	−1.40	0.11	−0.19
57		2XMM J094439.8+034940	53 143.621	0.155	0	0	29.31	25.30	−1.54	−0.18	−0.30
58		2XMM J095253.7+075040	52 402.926	1.468	0	0	31.12	26.59	−1.74	−0.05	0.16
59		2XMM J095815.5+014922	53 500.598	1.509	0	0	30.41	27.10	−1.27	0.29	−0.35
60		2XMM J095819.8+022903	53 312.266	0.345	0	0	29.32	25.43	−1.49	−0.13	−0.42
61		2XMM J095821.6+024628	53 348.320	1.403	1	0	30.56	26.70	−1.48	0.11	−0.35
62		2XMM J095834.0+024427	53 348.320	1.888	0	0	31.02	26.83	−1.61	0.06	−0.35
63	1	2XMM J095857.3+021314	52 984.953	1.024	0	0	29.78	27.09	−1.03	0.42	−0.29
63	2	2XMM J095857.3+021314	53 499.809	1.024	0	0	29.85	26.98	−1.10	0.36	−0.16
64	1	2XMM J095858.6+020139	53 351.918	2.454	0	0	31.05	26.99	−1.56	0.11	−0.49
64	2	2XMM J095858.6+020139	53 500.195	2.454	0	0	31.10	27.04	−1.56	0.12	−0.47
65		2XMM J095902.7+021906	52 984.953	0.345	0	0	28.94	26.00	−1.13	0.17	−0.34
66		2XMM J095908.3+024309	53 701.762	1.317	1	0	30.57	27.19	−1.30	0.29	−0.30
67		2XMM J095918.7+020951	52 984.953	1.157	1	0	30.03	26.81	−1.24	0.25	−0.28
68		2XMM J095924.4+015954	53 351.918	1.236	0	0	30.95	26.65	−1.65	0.01	−0.40
69		2XMM J095946.0+024743	53 701.762	1.067	0	0	30.65	26.42	−1.62	−0.02	−0.43
70		2XMM J095949.4+020141	53 351.918	1.753	0	0	30.94	25.61	−2.05	−0.40	−0.76
71		2XMM J095958.0+014327	53 328.664	1.618	0	0	30.56	25.72	−1.86	−0.27	−0.63
72		2XMM J100001.3+024845	53 340.984	0.766	0	0	29.99	26.04	−1.52	−0.04	−0.40
73	1	2XMM J100012.9+023522	52 981.777	0.699	0	0	30.03	26.12	−1.50	−0.01	−0.42
73	2	2XMM J100012.9+023522	53 340.984	0.699	0	0	30.13	26.04	−1.57	−0.06	−0.56
73	3	2XMM J100012.9+023522	53 697.477	0.699	0	0	29.84	25.99	−1.48	−0.02	−0.56
74		2XMM J100024.3+015053	52 983.094	1.664	0	0	30.35	26.42	−1.51	0.04	−0.29
75	1	2XMM J100024.6+023148	52 981.777	1.318	0	0	30.75	26.47	−1.64	−0.02	−0.40
75	2	2XMM J100024.6+023148	53 697.477	1.318	0	0	30.72	26.25	−1.71	−0.10	−0.45
76		2XMM J100025.2+015852	52 983.094	0.373	0	0	29.39	26.00	−1.30	0.08	−0.35
77	1	2XMM J100043.1+020637	52 983.484	0.360	0	0	28.98	25.43	−1.36	−0.06	−0.41
77	2	2XMM J100043.1+020637	53 697.738	0.360	0	0	29.05	25.41	−1.40	−0.08	−0.11
78		2XMM J100058.8+015359	53 329.047	1.559	0	0	30.36	26.65	−1.42	0.13	−0.17
79	1	2XMM J100114.3+022356	52 979.078	1.799	0	0	30.93	26.56	−1.68	−0.03	−0.40
79	2	2XMM J100114.3+022356	53 697.227	1.799	0	0	30.88	26.61	−1.64	0.00	−0.24
80		2XMM J100116.7+014053	53 331.000	2.055	0	0	30.95	26.30	−1.78	−0.12	−0.49
81	1	2XMM J100120.2+023341	52 979.078	1.834	0	0	30.65	26.11	−1.74	−0.14	−0.39
81	2	2XMM J100120.2+023341	53 697.227	1.834	0	0	30.82	26.49	−1.66	−0.03	−0.42
82		2XMM J100130.3+014304	53 331.000	1.571	0	0	30.46	26.25	−1.62	−0.05	−0.18
83		2XMM J100132.2+013419	53 331.000	1.360	0	0	30.35	26.09	−1.63	−0.08	−0.23
84		2XMM J100205.2+554258	52 926.145	1.151	0	0	30.79	26.55	−1.63	−0.00	0.35
85	1	2XMM J100219.5+015537	53 330.234	1.509	0	0	30.29	26.06	−1.62	−0.08	−0.57
85	2	2XMM J100219.5+015537	53 696.145	1.509	0	0	30.42	26.13	−1.65	−0.09	−0.62
86		2XMM J100226.3+021923	53 504.160	1.294	0	0	30.17	26.41	−1.44	0.08	−0.41
87	1	2XMM J100232.1+023537	53 350.574	0.658	0	0	30.00	25.98	−1.54	−0.05	−0.47
87	2	2XMM J100232.1+023537	53 695.887	0.658	0	0	29.89	25.93	−1.52	−0.05	−0.52
88	1	2XMM J100234.3+015011	53 330.234	1.506	0	0	30.93	26.43	−1.73	−0.08	−0.52
88	2	2XMM J100234.3+015011	53 693.703	1.506	0	0	30.95	26.61	−1.66	−0.00	−0.38
89		2XMM J100236.6+015949	53 330.234	1.516	0	0	30.60	26.11	−1.72	−0.13	−0.27
90	1	2XMM J100238.2+013747	53 330.621	2.506	0	0	31.23	26.96	−1.64	0.06	−0.21
90	2	2XMM J100238.2+013747	53 693.703	2.506	0	0	31.29	26.71	−1.76	−0.04	−0.54
91		2XMM J100248.9+325130	53 677.328	1.537	0	0	30.68	26.87	−1.46	0.15	−0.39
92		2XMM J100325.0+325305	53 677.328	2.511	0	0	31.29	26.47	−1.85	−0.13	−0.31
93		2XMM J100441.0+410944	53 115.141	1.022	0	0	30.63	25.84	−1.84	−0.24	−0.34
94		2XMM J100717.2+124543	52 763.820	1.281	0	0	31.21	26.79	−1.70	0.00	−0.39
95		2XMM J100726.0+124856	52 763.820	0.241	1	1	30.46	25.70	−1.83	−0.26	−0.15
96		2XMM J101148.9+554102	52 224.977	1.533	0	0	30.72	26.51	−1.61	0.00	−0.27
97		2XMM J101720.6+385738	52 215.426	0.629	0	0	29.77	26.27	−1.34	0.11	−0.33
98		2XMM J101850.4+411508	52 216.008	0.577	0	0	30.24	26.41	−1.47	0.06	−0.46
99		2XMM J101857.5+412549	52 216.008	2.123	0	0	30.69	26.73	−1.52	0.09	−0.18

Table 1. continued.

N_{sou} (1)	N_{epo} (2)	Source (3)	Epoch (4)	z (5)	f_{RL} [a] (6)	f_{BAL} [b] (7)	$\log L_{UV}$ (8)	$\log L_X$ (9)	α_{ox} (10)	$\Delta\alpha_{ox}$ (11)	$HR3$ (12)
100		2XMM J102003.7+081837	52 055.531	2.094	0	0	30.81	27.24	−1.37	0.26	−0.24
101		2XMM J102117.7+131546	52 764.246	1.565	0	0	31.00	26.73	−1.64	0.02	−0.53
102		2XMM J102124.9+130115	52 764.246	1.007	0	0	30.41	26.46	−1.52	0.04	−0.44
103		2XMM J102147.4+130850	52 764.246	0.656	0	0	30.05	26.35	−1.42	0.07	−0.38
104		2XMM J102350.9+041542	51 883.770	1.809	0	0	30.93	26.46	−1.72	−0.07	−0.28
105		2XMM J103031.6+052455	52 781.621	1.183	0	0	31.36	26.48	−1.87	−0.14	−0.38
106		2XMM J103216.0+505119	53 473.809	0.173	0	0	29.15	25.63	−1.35	−0.02	−0.11
107		2XMM J103338.7+004226	53 715.141	0.361	0	0	29.10	24.88	−1.62	−0.29	−0.62
108		2XMM J103413.9+585252	52 930.035	0.745	0	0	30.78	26.33	−1.71	−0.09	−0.46
109		2XMM J103922.6+643417	53 677.684	2.128	−1	0	31.19	26.74	−1.71	−0.01	−0.19
110		2XMM J103935.7+533039	52 040.297	0.229	0	0	28.79	25.43	−1.29	−0.02	−0.36
111		2XMM J103951.5+643005	53 677.684	0.402	1	0	28.82	24.24	−1.76	−0.48	−0.41
112		2XMM J104155.7+061256	52 777.816	1.478	0	0	30.62	26.01	−1.77	−0.17	−0.46
113		2XMM J104542.2+525112	53 303.078	1.058	1	0	30.85	27.30	−1.37	0.27	−0.37
114		2XMM J104609.8+530008	53 303.078	1.179	0	0	30.61	26.41	−1.61	−0.02	−0.27
115		2XMM J104613.6+525554	53 303.078	0.503	0	0	30.31	26.14	−1.60	−0.06	−0.66
116	1	2XMM J105039.5+572336	52 562.273	1.447	1	0	30.52	26.66	−1.48	0.10	−0.30
116	2	2XMM J105039.5+572336	52 564.340	1.447	1	0	30.51	26.54	−1.52	0.06	−0.44
117		2XMM J105143.8+335927	52 407.168	0.167	0	0	29.65	26.04	−1.39	0.03	−0.39
118		2XMM J105204.5+440152	52 754.262	1.524	0	0	30.83	26.64	−1.61	0.02	−0.12
119	1	2XMM J105221.0+440439	52 754.262	0.968	0	0	30.80	26.06	−1.82	−0.19	−0.47
119	2	2XMM J105221.0+440439	52 783.555	0.968	0	0	30.85	26.31	−1.74	−0.10	−0.43
120	1	2XMM J105224.9+441505	52 754.262	0.443	0	0	29.48	26.29	−1.23	0.16	−0.37
120	2	2XMM J105224.9+441505	52 783.555	0.443	0	0	29.40	26.15	−1.25	0.13	−0.43
121	1	2XMM J105239.6+572431	51 661.148	1.112	0	0	30.91	26.67	−1.63	0.02	−0.41
121	2	2XMM J105239.6+572431	52 209.797	1.112	0	0	30.78	26.82	−1.52	0.10	−0.43
121	3	2XMM J105239.6+572431	52 217.285	1.112	0	0	30.78	26.81	−1.52	0.10	−0.36
121	4	2XMM J105239.6+572431	52 566.344	1.112	0	0	30.72	26.70	−1.54	0.07	−0.33
121	5	2XMM J105239.6+572431	52 568.359	1.112	0	0	30.73	26.75	−1.53	0.09	−0.41
121	6	2XMM J105239.6+572431	52 570.340	1.112	0	0	30.73	26.79	−1.51	0.11	−0.42
121	7	2XMM J105239.6+572431	52 605.977	1.112	0	0	30.74	26.70	−1.55	0.07	−0.40
121	8	2XMM J105239.6+572431	52 612.199	1.112	0	0	30.73	26.72	−1.54	0.08	−0.40
121	9	2XMM J105239.6+572431	52 614.160	1.112	0	0	30.73	26.75	−1.53	0.09	−0.38
122	1	2XMM J105316.7+573550	51 661.148	1.205	0	0	30.00	27.10	−1.11	0.38	−0.30
122	2	2XMM J105316.7+573550	52 570.340	1.205	0	0	30.21	26.99	−1.24	0.28	−0.30
122	3	2XMM J105316.7+573550	52 572.340	1.205	0	0	30.19	27.00	−1.23	0.29	−0.29
122	4	2XMM J105316.7+573550	52 605.977	1.205	0	0	30.26	27.04	−1.23	0.30	−0.29
122	5	2XMM J105316.7+573550	52 614.160	1.205	0	0	30.23	27.11	−1.20	0.33	−0.26
123		2XMM J110334.7+355108	52 044.387	1.200	0	0	30.05	25.89	−1.60	−0.11	−0.61
124		2XMM J111038.5+483116	52 426.695	2.955	0	0	32.01	27.26	−1.83	0.01	−0.44
125		2XMM J111706.4+441333	52 408.680	0.144	0	0	29.71	26.06	−1.40	0.03	−0.10
126		2XMM J111753.3+412016	53 715.844	2.221	1	0	31.13	27.59	−1.36	0.33	−0.33
127		2XMM J111830.2+402554	52 411.293	0.155	0	0	29.92	25.99	−1.51	−0.04	−0.53
128		2XMM J112026.2+134024	51 875.809	0.982	0	0	30.32	26.57	−1.44	0.10	−0.39
129		2XMM J112048.9+133822	51 875.809	0.513	0	0	29.64	25.04	−1.76	−0.34	−0.02
130		2XMM J112611.6+425245	51 871.109	0.156	0	0	28.68	23.82	−1.86	−0.61	0.52
131		2XMM J113109.4+311405	51 870.762	0.290	1	0	30.30	26.82	−1.33	0.21	−0.36
132	1	2XMM J113224.0+525157	53 127.523	0.837	0	0	30.14	26.06	−1.56	−0.05	−0.21
132	2	2XMM J113224.0+525157	53 313.078	0.837	0	0	30.01	25.88	−1.59	−0.10	−0.48
133		2XMM J114856.5+525426	53 313.254	1.633	1	0	31.77	27.88	−1.49	0.31	−0.25
134		2XMM J115838.5+435505	53 687.480	1.208	1	0	30.33	26.31	−1.54	0.00	−0.20
135		2XMM J115851.0+435048	53 687.480	0.287	0	0	29.02	25.42	−1.38	−0.07	−0.47
136		2XMM J120504.4+352209	52 782.684	2.279	0	0	31.55	26.98	−1.75	0.01	−0.30
137		2XMM J120522.1+443141	52 801.723	1.921	0	1	31.06	26.61	−1.71	−0.04	−0.07
138		2XMM J121342.9+025248	52 273.520	0.641	0	0	29.65	25.50	−1.59	−0.17	−0.61
139	1	2XMM J121426.5+140259	52 075.359	1.279	1	0	30.36	27.15	−1.23	0.32	−0.31
139	2	2XMM J121426.5+140259	53 177.242	1.279	1	0	30.40	27.23	−1.22	0.34	−0.30
140		2XMM J121640.5+071224	53 165.395	0.586	0	0	30.72	26.77	−1.52	0.09	−0.42
141		2XMM J121713.1+070236	53 165.395	1.203	0	0	30.73	26.59	−1.59	0.03	−0.58
142		2XMM J121919.0+063926	52 626.047	0.654	0	0	29.78	25.93	−1.48	−0.03	−0.44

Table 1. continued.

N_{sou} (1)	N_{epo} (2)	Source (3)	Epoch (4)	z (5)	f_{RL}[a] (6)	f_{BAL}[b] (7)	log L_{UV} (8)	log L_X (9)	α_{ox} (10)	$\Delta\alpha_{ox}$ (11)	$HR3$ (12)
143		2XMM J122018.4+064120	52 460.359	0.286	0	0	29.63	26.46	−1.22	0.20	−0.38
144		2XMM J122528.4+131725	53 366.883	1.794	0	0	31.60	26.54	−1.94	−0.17	−0.43
145		2XMM J122556.1+130656	52 456.777	1.350	0	0	30.68	26.50	−1.60	0.01	−0.26
146		2XMM J122703.3+125402	53 358.168	1.278	0	0	30.59	26.15	−1.70	−0.11	−0.37
147		2XMM J122742.9+013438	52 083.336	1.279	0	0	30.54	26.54	−1.53	0.05	−0.24
148		2XMM J122923.7+075359	52 430.555	0.854	0	0	29.79	26.53	−1.25	0.20	−0.30
149	1	2XMM J123049.7+640848	51 685.082	1.040	−1	0	30.35	26.18	−1.60	−0.05	−0.50
149	2	2XMM J123049.7+640848	52 760.367	1.040	−1	0	30.32	25.77	−1.74	−0.20	−0.37
150	1	2XMM J123054.1+110011	52 833.379	0.236	0	0	29.95	26.36	−1.38	0.10	−0.42
150	2	2XMM J123054.1+110011	53 717.434	0.236	0	0	30.03	26.28	−1.44	0.05	−0.42
150	3	2XMM J123054.1+110011	53 721.234	0.236	0	0	30.02	26.30	−1.43	0.06	−0.43
151	1	2XMM J123229.6+641115	51 685.082	0.743	0	0	30.39	25.95	−1.70	−0.14	−0.40
151	2	2XMM J123229.6+641115	52 760.367	0.743	0	0	30.45	26.26	−1.61	−0.04	−0.42
152		2XMM J123335.1+475801	53 173.680	0.382	0	0	30.19	26.65	−1.36	0.16	−0.47
153		2XMM J123356.1+074755	53 161.492	0.371	0	0	29.31	26.13	−1.22	0.14	−0.39
154		2XMM J123413.4+475352	53 173.680	0.373	1	0	30.05	26.27	−1.45	0.04	−0.49
155		2XMM J123508.2+393019	53 149.184	0.968	0	0	30.03	25.87	−1.60	−0.11	−0.42
156		2XMM J123527.3+392824	53 149.184	2.158	0	0	31.04	26.97	−1.56	0.11	−0.34
157	1	2XMM J123622.9+621526	52 047.398	2.587	0	0	30.79	26.81	−1.53	0.10	−0.17
157	2	2XMM J123622.9+621526	52 047.977	2.587	0	0	30.77	26.65	−1.58	0.04	−0.42
157	3	2XMM J123622.9+621526	52 056.293	2.587	0	0	30.55	26.70	−1.48	0.10	−0.35
157	4	2XMM J123622.9+621526	52 061.379	2.587	0	0	30.55	26.68	−1.49	0.09	−0.37
157	5	2XMM J123622.9+621526	52 967.422	2.587	0	0	30.57	26.02	−1.75	−0.16	−0.84
157	6	2XMM J123622.9+621526	52 987.977	2.587	0	0	30.46	26.51	−1.51	0.06	−0.08
158	1	2XMM J123759.5+621102	52 047.398	0.910	0	0	30.51	26.65	−1.48	0.10	−0.35
158	2	2XMM J123759.5+621102	52 047.977	0.910	0	0	30.49	26.72	−1.45	0.12	−0.30
158	3	2XMM J123759.5+621102	52 056.293	0.910	0	0	30.53	26.58	−1.52	0.06	−0.39
158	4	2XMM J123759.5+621102	52 061.379	0.910	0	0	30.52	26.59	−1.51	0.07	−0.33
158	5	2XMM J123759.5+621102	52 967.422	0.910	0	0	30.31	26.43	−1.49	0.05	−0.23
159	1	2XMM J123800.9+621336	52 047.398	0.440	0	0	29.59	25.58	−1.54	−0.13	−0.53
159	2	2XMM J123800.9+621336	52 047.977	0.440	0	0	29.57	25.48	−1.57	−0.16	−0.55
159	3	2XMM J123800.9+621336	52 056.293	0.440	0	0	29.57	25.33	−1.63	−0.22	−0.46
159	4	2XMM J123800.9+621336	52 061.379	0.440	0	0	29.55	25.50	−1.56	−0.15	−0.47
159	5	2XMM J123800.9+621336	52 967.422	0.440	0	0	29.48	25.42	−1.56	−0.17	−0.24
159	6	2XMM J123800.9+621336	52 979.543	0.440	0	0	29.46	25.33	−1.58	−0.19	−0.32
160		2XMM J124406.9+113524	51 911.711	1.344	0	0	30.26	26.80	−1.33	0.20	−0.37
161		2XMM J124540.9−002744	52 452.605	1.693	0	0	31.07	27.29	−1.45	0.23	−0.33
162		2XMM J124728.5+671725	53 703.648	1.220	−1	0	30.57	26.43	−1.59	−0.00	−0.38
163		2XMM J125535.1+565238	52 067.582	1.803	0	0	30.84	26.33	−1.73	−0.09	−0.52
164		2XMM J125536.2+564959	52 067.582	1.374	0	0	30.24	25.94	−1.65	−0.12	0.08
165		2XMM J125642.1+564719	52 067.582	1.956	0	0	30.62	26.50	−1.58	0.02	−0.45
166		2XMM J125840.2+283426	51 719.062	1.321	0	0	30.66	26.03	−1.78	−0.18	−0.27
167		2XMM J125849.8−014303	52 272.977	0.967	0	0	31.13	26.98	−1.59	0.10	−0.44
168	1	2XMM J125903.9+344702	52 804.578	0.608	0	0	29.79	26.20	−1.38	0.07	−0.34
168	2	2XMM J125903.9+344702	52 976.324	0.608	0	0	29.41	25.94	−1.33	0.05	−0.35
169	1	2XMM J130028.5+283010	52 432.785	0.649	1	0	30.57	27.02	−1.36	0.23	−0.34
169	2	2XMM J130028.5+283010	53 162.824	0.649	1	0	30.73	27.05	−1.41	0.21	−0.35
169	3	2XMM J130028.5+283010	53 174.715	0.649	1	0	30.73	27.08	−1.40	0.22	−0.34
169	4	2XMM J130028.5+283010	53 198.680	0.649	1	0	30.73	27.11	−1.39	0.23	−0.37
170	1	2XMM J130048.1+282321	52 432.785	1.924	0	0	31.58	26.83	−1.82	−0.05	−0.43
170	2	2XMM J130048.1+282321	53 162.824	1.924	0	0	31.44	26.66	−1.84	−0.10	−0.35
170	3	2XMM J130048.1+282321	53 174.715	1.924	0	0	31.43	26.62	−1.85	−0.11	−0.34
170	4	2XMM J130048.1+282321	53 198.680	1.924	0	0	31.43	26.64	−1.84	−0.10	−0.41
171		2XMM J130257.8+673006	52 381.281	1.837	1	0	31.03	26.84	−1.61	0.06	−0.27
172		2XMM J130454.3+673007	52 381.281	0.539	−1	0	29.59	25.80	−1.46	−0.05	−0.37
173		2XMM J130942.2−014139	53 539.754	0.824	0	0	30.26	25.71	−1.75	−0.22	−0.31
174		2XMM J130952.0−013217	53 539.754	1.844	1	0	30.57	26.78	−1.45	0.14	−0.26
175		2XMM J131817.6+324053	52 465.020	1.647	0	0	31.33	27.05	−1.64	0.08	−0.39
176		2XMM J132419.8+053704	53 197.707	0.203	1	0	28.80	23.65	−1.98	−0.71	−0.54
177		2XMM J132607.0+655543	53 125.266	1.513	−1	0	30.99	26.52	−1.72	−0.06	−0.37

Table 1. continued.

N_{sou} (1)	N_{epo} (2)	Source (3)	Epoch (4)	z (5)	f_{RL}[a] (6)	f_{BAL}[b] (7)	$\log L_{UV}$ (8)	$\log L_X$ (9)	α_{ox} (10)	$\Delta\alpha_{ox}$ (11)	$HR3$ (12)
178		2XMM J132623.0+011501	53 370.500	1.232	0	0	30.43	26.12	−1.65	−0.09	−0.32
179		2XMM J132711.1+011010	53 370.500	0.971	0	0	30.54	26.34	−1.61	−0.03	−0.36
180		2XMM J133526.7+405958	52 621.199	1.765	0	0	31.16	26.65	−1.73	−0.04	−0.06
181		2XMM J134044.5−004516	53 549.691	0.386	0	0	30.03	25.99	−1.55	−0.06	−0.40
182		2XMM J134113.9−005314	53 549.691	0.237	1	0	29.39	26.41	−1.14	0.24	−0.36
183		2XMM J134252.9+403202	52 433.379	0.906	1	0	29.78	26.74	−1.17	0.28	−0.26
184	1	2XMM J134256.5+000057	52 482.906	0.804	0	0	30.01	26.64	−1.30	0.19	−0.22
184	2	2XMM J134256.5+000057	53 033.730	0.804	0	0	29.90	26.69	−1.23	0.24	−0.34
185		2XMM J134740.9+581242	52 066.254	2.050	1	0	31.66	27.64	−1.54	0.24	−0.36
186		2XMM J134749.8+582109	52 066.254	0.646	0	0	30.83	27.08	−1.44	0.19	−0.37
187		2XMM J134834.2+262205	52 652.574	0.918	0	0	30.42	26.54	−1.49	0.07	−0.59
188		2XMM J134848.2+262219	52 652.574	0.595	0	0	30.06	26.07	−1.53	−0.03	−0.46
189		2XMM J135639.1+051950	53 213.418	1.394	0	0	30.49	26.76	−1.43	0.14	−0.46
190		2XMM J140040.4+621243	53 109.504	0.661	0	0	29.48	25.79	−1.42	−0.03	−0.58
191	1	2XMM J141642.3+521813	51 746.934	1.285	0	0	31.01	26.38	−1.78	−0.11	−0.28
191	2	2XMM J141642.3+521813	51 748.750	1.285	0	0	31.00	26.39	−1.77	−0.11	−0.12
191	3	2XMM J141642.3+521813	51 748.926	1.285	0	0	30.98	26.51	−1.72	−0.06	−0.10
192		2XMM J141700.7+445606	52 616.805	0.114	0	0	29.39	25.61	−1.45	−0.07	−0.47
193		2XMM J142355.5+383150	53 528.645	1.205	0	0	30.45	26.32	−1.59	−0.02	−0.71
194		2XMM J142406.6+383714	52 851.906	1.561	0	0	31.02	26.62	−1.69	−0.02	−0.58
195	1	2XMM J142435.9+421030	52 848.184	2.218	0	0	31.68	27.37	−1.65	0.14	−0.25
195	2	2XMM J142435.9+421030	52 991.941	2.218	0	0	31.63	27.14	−1.72	0.06	−0.44
196	1	2XMM J142455.5+421408	52 848.184	0.316	0	0	30.29	26.27	−1.54	−0.00	−0.45
196	2	2XMM J142455.5+421408	52 991.941	0.316	0	0	30.22	26.28	−1.51	0.02	−0.41
197		2XMM J142904.3+012228	51 753.441	0.420	0	0	29.34	25.87	−1.34	0.03	−0.28
198		2XMM J142917.6+012059	51 753.441	1.133	0	0	30.59	26.40	−1.61	−0.02	−0.35
199		2XMM J142931.5+012124	51 753.441	1.518	0	0	30.69	26.46	−1.62	−0.01	−0.55
200		2XMM J142943.0+474726	52 425.266	0.221	0	0	29.91	26.23	−1.41	0.06	−0.44
201	1	2XMM J143025.8+415957	52 617.281	0.352	0	0	29.26	25.82	−1.32	0.03	−0.43
201	2	2XMM J143025.8+415957	52 656.703	0.352	0	0	29.12	25.84	−1.26	0.07	−0.38
202		2XMM J143424.9+033912	53 600.020	1.120	0	0	30.61	26.42	−1.61	−0.02	−0.38
203		2XMM J143440.4+484139	52 647.297	1.945	0	0	31.11	25.97	−1.97	−0.29	−0.75
204		2XMM J143506.5+033258	53 600.020	2.404	0	0	30.90	26.85	−1.55	0.10	−0.34
205		2XMM J143513.9+484149	52 647.297	1.887	0	1	30.54	26.82	−1.43	0.15	−0.36
206		2XMM J143621.2+484606	52 647.297	2.395	0	0	31.15	26.58	−1.76	−0.07	−0.72
207		2XMM J143822.0+642000	51 908.621	1.163	−1	0	30.69	26.46	−1.63	−0.02	−0.40
208		2XMM J144414.6+063306	53 412.715	0.208	0	0	29.64	26.49	−1.21	0.21	−0.38
209		2XMM J144645.9+403506	52 497.062	0.267	0	0	30.39	26.13	−1.63	−0.07	−0.54
210		2XMM J150121.9+014401	53 574.242	0.608	1	0	29.18	26.36	−1.08	0.26	0.06
211		2XMM J150148.8+014403	53 574.242	0.484	0	0	29.45	25.79	−1.40	−0.01	−0.37
212		2XMM J150948.6+333626	52 852.219	0.512	0	0	29.40	25.45	−1.52	−0.14	−0.46
213		2XMM J151443.0+365050	52 511.234	0.371	1	0	30.41	26.95	−1.33	0.23	−0.38
214		2XMM J151551.6+000304	53 209.027	1.775	0	0	30.96	26.29	−1.79	−0.13	0.02
215		2XMM J151630.2−010108	53 220.680	1.212	0	0	30.37	26.20	−1.60	−0.05	−0.48
216		2XMM J151630.2−005625	53 220.680	1.921	1	1	30.98	26.77	−1.62	0.04	−0.34
217		2XMM J151652.7−005834	53 220.680	1.722	0	0	31.10	26.89	−1.62	0.06	−0.29
218		2XMM J151842.8+424933	53 245.457	1.465	0	0	30.73	26.52	−1.62	−0.00	−0.14
219	1	2XMM J152553.8+513649	52 252.004	2.882	0	1	31.69	27.87	−1.47	0.32	−0.37
219	2	2XMM J152553.8+513649	52 256.246	2.882	0	1	31.64	27.84	−1.46	0.32	−0.39
220		2XMM J153322.8+324351	52 485.520	1.899	0	0	30.57	26.86	−1.42	0.17	−0.31
221		2XMM J153438.1+553945	52 411.594	1.130	0	0	30.26	26.43	−1.47	0.06	−0.50
222		2XMM J154530.3+484608	52 678.859	0.400	0	0	30.53	26.07	−1.71	−0.13	−0.57
223		2XMM J160106.2+084605	52 860.309	1.207	0	0	30.47	27.03	−1.32	0.25	−0.35
224		2XMM J160658.2+271706	53 580.660	0.934	1	0	30.41	27.22	−1.22	0.34	−0.20
225	1	2XMM J162855.6+394034	52 461.664	1.520	0	0	30.74	26.29	−1.71	−0.09	−0.66
225	2	2XMM J162855.6+394034	52 501.555	1.520	0	0	30.81	26.79	−1.54	0.09	−0.24
226		2XMM J164221.1+390333	53 237.520	1.713	0	0	30.95	26.78	−1.60	0.06	−0.34
227		2XMM J165713.2+352441	51 972.938	2.329	0	0	31.12	26.93	−1.61	0.08	−0.16
228		2XMM J170100.6+641208	52 425.770	2.736	−1	0	32.32	27.52	−1.84	0.06	−0.43
229	1	2XMM J170639.3+240606	52 707.043	0.836	0	0	29.67	25.90	−1.45	−0.02	−0.32

Table 1. continued.

N_{sou} (1)	N_{epo} (2)	Source (3)	Epoch (4)	z (5)	f_{RL}[a] (6)	f_{BAL}[b] (7)	log L_{UV} (8)	log L_X (9)	α_{ox} (10)	$\Delta\alpha_{ox}$ (11)	$HR3$ (12)
229	2	2XMM J170639.3+240606	52 864.641	0.836	0	0	29.56	26.01	−1.36	0.05	−0.13
230		2XMM J171359.4+640939	52 615.277	1.359	0	0	30.80	26.50	−1.65	−0.02	−0.58
231		2XMM J212909.6+001214	52 576.086	1.339	0	0	30.39	25.93	−1.71	−0.15	−0.58
232	1	2XMM J221738.4+001207	52 596.160	1.121	0	0	29.81	25.84	−1.52	−0.07	−0.40
232	2	2XMM J221738.4+001207	52 623.918	1.121	0	0	29.86	25.85	−1.54	−0.08	−0.39
233	1	2XMM J221751.3+001146	52 596.160	1.491	0	0	30.38	26.36	−1.55	0.00	−0.37
233	2	2XMM J221751.3+001146	52 623.918	1.491	0	0	30.39	26.36	−1.55	0.01	−0.39
234	1	2XMM J221755.2+001513	52 596.160	2.092	0	0	30.47	26.37	−1.57	−0.00	−0.39
234	2	2XMM J221755.2+001513	52 623.918	2.092	0	0	30.32	26.52	−1.46	0.08	−0.29
235		2XMM J223607.6+134355	52 787.641	0.326	−1	0	30.41	26.31	−1.57	−0.01	−0.50
236		2XMM J233706.4+002132	52 249.578	0.713	0	0	29.37	26.10	−1.25	0.12	−0.34
237		2XMM J233707.2+002007	52 249.578	1.901	0	0	31.11	26.70	−1.69	−0.01	−0.58
238		2XMM J233722.0+002238	52 249.578	1.376	0	0	30.46	26.00	−1.71	−0.14	−0.51
239		2XMM J234715.3+005808	52 636.617	1.487	0	0	30.22	26.66	−1.37	0.16	−0.48
240		2XMM J234715.9+005602	52 636.617	0.456	0	0	29.04	25.63	−1.31	0.01	−0.50
241		2XMM J234724.7+005248	52 636.617	1.323	1	0	30.53	26.98	−1.36	0.22	−0.28

Notes. [a] 1=radio-loud; 0=radio-quiet; -1=radio-unclassified.
[b] 1=BAL; 0=non-BAL .